

## Chapter 7<sup>1</sup>

# The 34-Meter Research and Development Beam-Waveguide Antenna

There are a number of advantages to feeding a large ground station antenna via a beam-waveguide (BWG) system rather than directly placing the feed at the focal point of a dual-reflector antenna. In a BWG system, the feed horn and support equipment are placed in a stationary room below the antenna, and the energy is guided from the feed horn to the subreflector, using a system of reflecting mirrors. Thus, significant simplifications are possible in the design of high-power water-cooled transmitters and low-noise cryogenic amplifiers, since these systems do not have to tilt as in normally fed dual-reflector antennas. Furthermore, these systems and other components can be placed in a more accessible location, enabling easier servicing and repair. In addition, the losses associated with rain on the feed-horn cover are eliminated because the feed horn is sheltered from weather.

Consequently, in the late 1980s, the National Aeronautics and Space Administration (NASA) Deep Space Network (DSN) undertook a comprehensive research program aimed at introducing BWG-fed antennas into the operational network. The research encompassed (a) new analytical techniques for predicting the performance of BWGs; (b) a model test facility to experimentally verify the analytical tools; and (c) the design, construction, and test of a new 34-m research and development (R&D) antenna.

Around the same time, various studies pointed to the advantage of using Ka-band (31.8–32.2 GHz receive and 34.2–34.7 GHz transmit) for the telecom-

---

<sup>1</sup>Based on “Evolution of the Deep Space Network 34-M Diameter Antennas,” by William A. Imbriale, which appeared in *Proceedings of the IEEE Aerospace Conference*, Snowmass, Colorado, March 21–28, 1998. (© 1998 IEEE)

munications link [1]. Therefore, the R&D antenna was designed to operate at Ka-band and thus be the testbed for introducing Ka-band frequencies into the operational network.

## 7.1 New Analytical Techniques

A BWG system consists of a number of conic-section mirrors enclosed in a metal tube. There is a feed horn on the input, and the output irradiates the sub-reflector of the dual-reflector system. The commonly used analysis of this system ignores the presence of the metallic tube enclosing the BWG mirrors and uses either physical optics (PO), the Geometrical Theory of Diffraction, or Gaussian-mode analysis of the diffracted field calculations. However, the basic weakness of these analyses is that they do not shed any light on the effect of the metal tube. Therefore, a new and fundamentally more correct BWG analysis that considers the presence of the metal tube was developed [2,3]. The basic concept is to use a Green's function appropriate to the circular-waveguide geometry to compute the scattered field. With the new analysis, an accurate assessment of the effects of the tube, including noise-temperature increase due to conduction losses in the tube, can be factored into the design. The technique is described in detail in Chapter 1 of this monograph.

## 7.2 Beam-Waveguide Test Facility

In support of analytical and test activities, a flexible test facility [4] was constructed to study BWG performance parameters. The objectives of the test facility were to (a) measure and characterize multiple mirror systems used in BWG antennas, (b) verify computer software and software models, (c) characterize BWG components not easily modeled by software, and (d) predict performance of BWG antenna designs.

The BWG test structure was installed in a microwave anechoic chamber 6 m wide by 6 m high and 18 m long. The test facility setup consists of (a) a structure to hold the BWG elements under test; (b) a test probe, mounted and independent of the BWG structure support, to provide the radiating patterning sampling device; and (c) an instrument control and its acquisition software. The test probe assembly consists of an open-ended circular-waveguide feed horn mounted at the end of a long radial arm that is rotated in a circular arc by a 20-cm optical-grade rotating table. The feed/arm/rotating table element is itself mounted in an azimuthal positioner. This design allows complete tangential field sampling over a hemispheric surface at a given radius from the center of

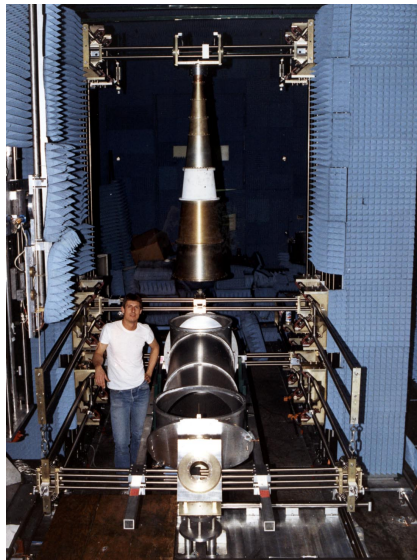


**Fig. 7-1. The BWG test facility with two-mirror configuration.**

the radial arm rotation point, thus producing a spherical near-field range measurement setup. A picture of the test facility is shown in Fig. 7-1.

One-quarter-scale mirrors (of those used in the full-scale 34-m R&D antenna) were machined from solid aluminum blocks and used in one-, two-, and three-mirror test configurations (see Figs. 7-1 through 7-3). The one-mirror beam-magnifier configuration results are shown in Fig. 7-4(a) for the offset plane (orthogonal to the plane of symmetry) at Ka-band. The beam-magnifier configuration consists of an ellipse and a 22-dB-gain input feed horn at one focal point that produces a 29-dB-gain output feed pattern at the second ellipse focal point. Compared are the computed and measured near-field results. Computations were made using a near-field PO program. The two-mirror results are shown in Fig. 7-4(b) for X-band (8.4 GHz) and Fig. 7-4(c) for Ka-band (32 GHz). The two-mirror system is a standard two-parabola configuration that replicates the input feed-horn pattern at the second parabola focal point. Three-mirror results are shown in Fig. 7-4(d) and consist of a 22-dB-gain input horn at the focal point of a beam-magnifier ellipse that produces a 29-dB output pattern for input to the standard two-mirror system. The excellent correlation that was achieved between measured and predicted results enabled the full-scale 34-m antenna system implementation to proceed with confidence.



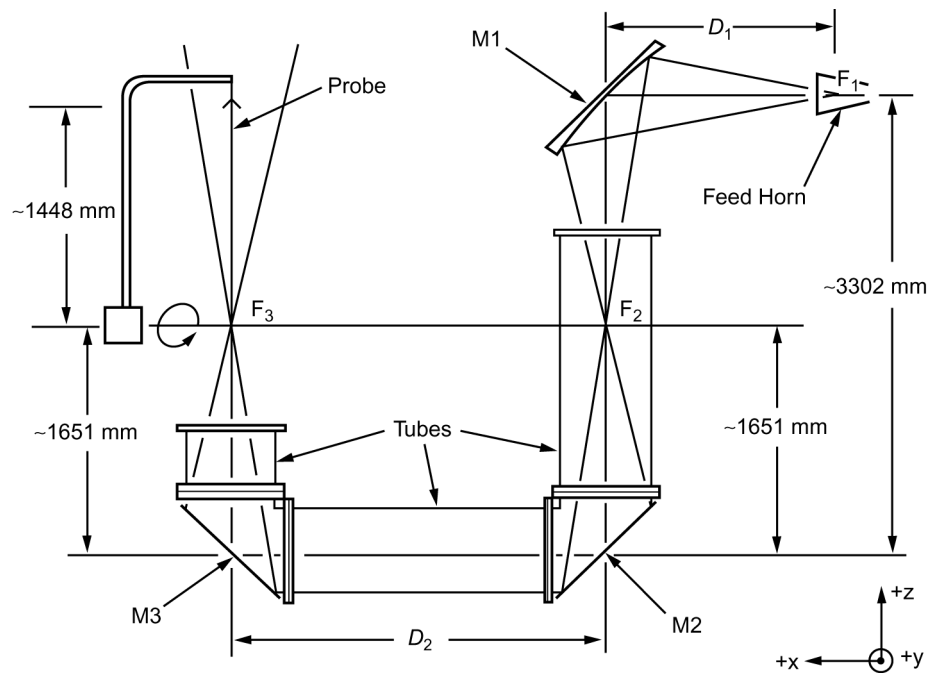
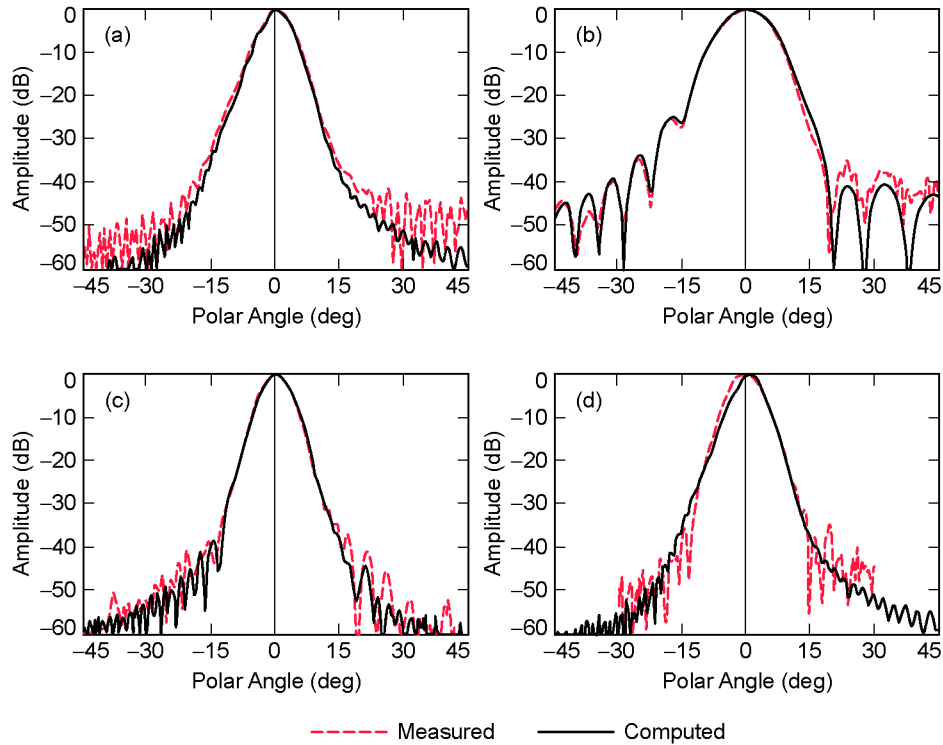


Fig. 7-3. Schematic of the three-mirror configuration.

design (see Fig. 7-7), places the BWG through the center of the dish, inside the elevation bearing and through the azimuth axis, into a pedestal room located below the antenna. The bypass design uses a single pair of paraboloids and two flat mirrors whereas the center design uses the same design (although not physically the same mirrors) above the ground, and a flat plate and beam-magnifier ellipse in the pedestal room. A beam magnifier is required, since the pair of paraboloids requires the use of a 29-dB-gain feed horn that at lower frequencies would be too large to fit into the pedestal room. The ellipse design allows the use of a smaller-gain feed horns in the pedestal room.

### 7.3.1 Antenna Design Considerations

At present, the DSN operates three 34-m high-efficiency (HEF) dual-shaped reflector antennas, each with a dual-band (2.3- and 8.4-GHz) feed horn having a far-field gain of 22.4 dBi (see Chapter 6 of this monograph for a full discussion of the first HEF antenna, DSS-15). The feed horn is conventionally located at the Cassegrain focal point. The structures were designed prior to BWG requirements, and therefore feature a continuous elevation axle and a carefully designed elevation-wheel substructure. The elevation wheel is supported by an alidade, which rotates on a circular azimuth track. To minimize



**Fig. 7-4.** Measured and computed data for the offset plane: (a) one-mirror, Ka-band; (b) two-mirror, X-band; (c) two-mirror, Ka-band; and (d) three-mirror, Ka-band.

the cost of developing a new 34-m BWG antenna, as much of the existing structure design as possible was used. Through the use of a clever mechanical design, the elevation tipping structure was modified to accommodate a central BWG inside the elevation bearing. To provide clear access for an 8-ft- (2.438-m)-diameter, center-fed BWG, the main reflector backup trusses are connected to the elevation wheel via the integral ring girder, or IRG. The IRG is a toroidal structure—an octagonal space truss with a square cross-section, approximately 290 in. (7.366 m) in maximum radius and 80 in. (2.032 m) high. It is interwoven with, but separate from, the antenna backup structure. In order to minimize the distortion of the reflector's surface under gravity loading, the reflector connections to the elevation-wheel structure were selected to provide equal stiffness supports. This is achieved by grouping either equally spaced reflector radial ribs into four pairs and connecting each pair to the IRG top plane at alternate vertices of the octagon. The vertices lying on the elevation axis, however, are reserved for supporting the IRG at the two elevation bearing points. The counterweight and single elevation bullgear lie in a plane orthogo-



**Fig. 7-5. The beam-waveguide antenna after construction in 1990.**

nal to the elevation axis. The entire tipping structure, including the main reflector, elevation wheel, subreflector and its support, is weight balanced about the elevation axis.

By selecting the existing HEF reflector structure design, the focal length over diameter ( $F/D$ ) of the main reflector surface is fixed. The reflector shape could be different than that for the original HEF design but would have to be within an adjustable tolerance  $\sim 1$  in. ( $\sim 2.5$  cm) of the existing surface.

### 7.3.2 Upper-Mirror Optics Design

Geometrical optics is used to design the upper portion of the centerline BWG system (mirrors M1 to M4). As shown in Fig. 7-7, the first mirror, M1, has azimuth and elevation rotations together with the main and subreflectors. A plane surface is used for M1 to ensure an imaged feed pattern that is independent of the elevation angle of the antenna. Mirrors M2 and M3 are parabolas, and the system is designed such that a feed horn placed at  $F_2$  is perfectly imaged at  $F_1$  [8]. Mirrors M2 through M4 rotate in azimuth around the centerline axis.

An imaged feed pattern at  $F_1$  is used to illuminate a subreflector with a narrow-angle, high-gain ( $\sim 30$ -dBi) pattern. This configuration is chosen because of the large distance between the subreflector and the first BWG mirror (M1), and also because the size of M1 (as well as M2) is smaller than the subreflector. The position of focal point  $F_1$  in Fig. 7-7 has to be closer to M1 in order to

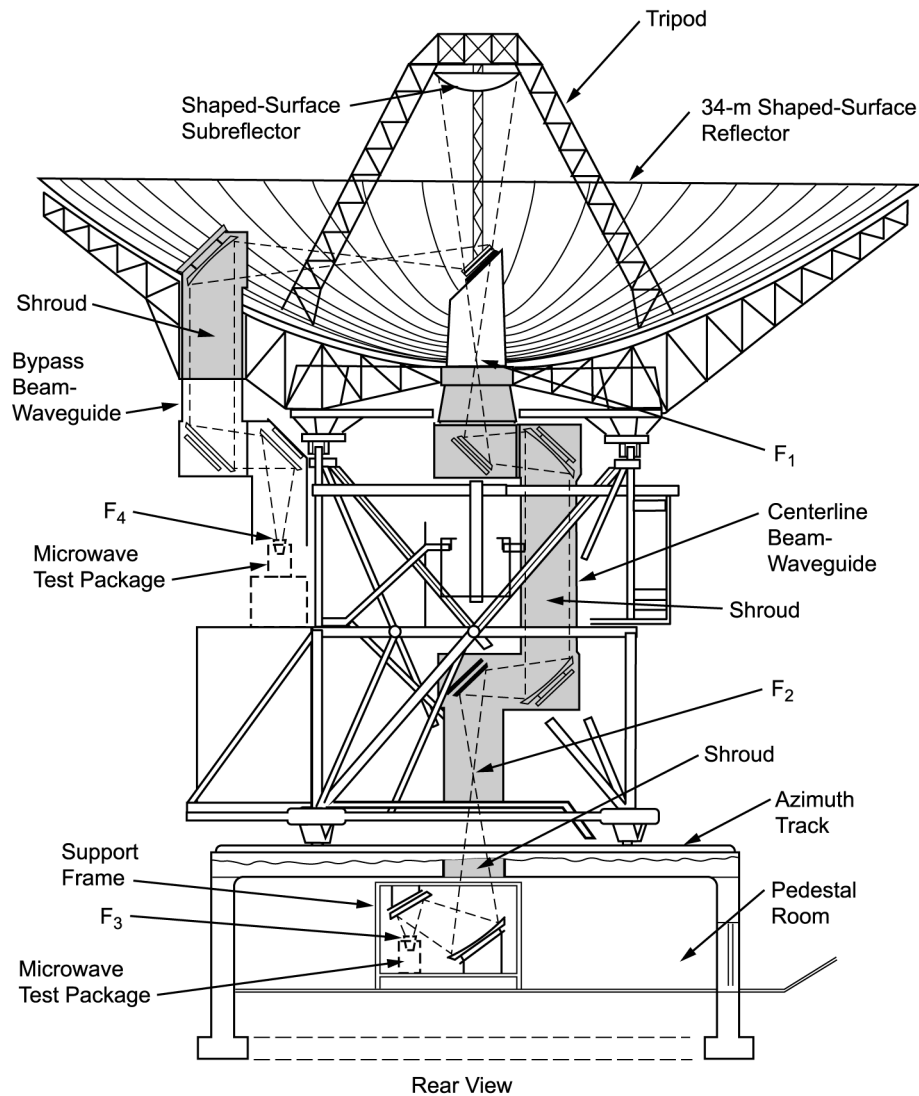


**Fig. 7-6. Beam-waveguide schematic.**

achieve acceptable spillover loss at the subreflector, M1, and M2. Normally,  $F_1$  is in the neighborhood of the main reflector vertex with an 8- to 9-deg half-cone angle of illumination at the subreflector (compared to 17 deg for the normal Cassegrain feed of the 34-m HEF antenna).

The diameter of the subreflector,  $D_s$ , is determined according to the size of the main reflector. According to [9], a subreflector diameter of 1/10 of a main reflector is normally selected for good radiation efficiency of the antenna. For a 34-m antenna, the subreflector diameter of 135 in. (3.42 m) was chosen. The



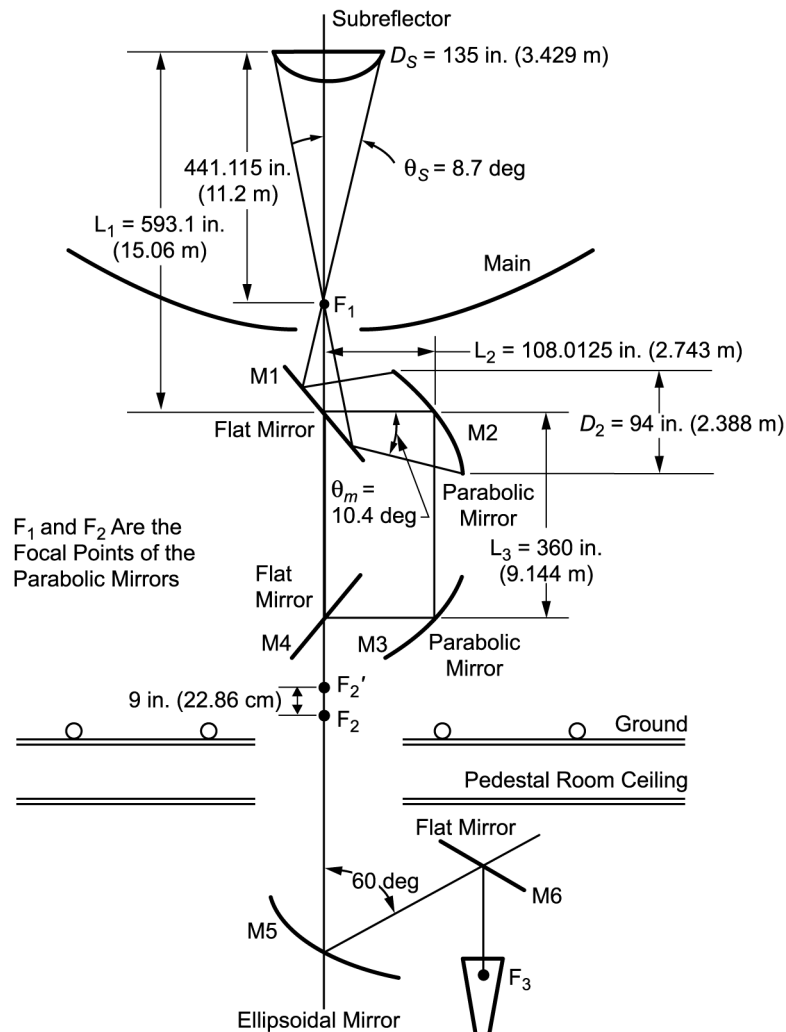


**Fig. 7-7. Center-fed beam-waveguide layout.  $F_1$  and  $F_2$  are the focal points of the parabolic mirrors.  $F_3$  and  $F_2'$  are the focal points of the ellipsoidal mirror.**

illumination at the subreflector  $\theta_s$  is 8.7 deg. (compared to 17 deg for the normal Cassegrain feed of the 34-m HEF antenna).

For the same ratio as the HEF antenna and where  $D_s = 135 \text{ in. (3.42 m)}$ , the distance  $L_1 = 593.1 \text{ in. (15.065 m)}$  is obtained. Iterations are needed for a determination of  $\theta_s$  and the location  $F_1$ . Known parameters are

$$D_s = 135 \text{ in. (3.42 m)}$$

$$L_1 = 593.1 \text{ in. (15.065 m)}$$

$$D_2 = 94 \text{ in. (2.388 m)}$$

Variable parameters are

$$8.0 \text{ deg} < \theta_s < 9.0 \text{ deg}$$

$$2.67 \text{ m} < L_2 < 2.8 \text{ m}$$

$$9.5 \text{ deg} < \theta_m < 11.0 \text{ deg.}$$

The angle  $\theta_m$  is the illumination angle at M2 with an edge taper of about  $-23$  dB. The results of iterations of a GO ray geometry between  $D_s$  and  $D_2$  are

$$\theta_s = 8.7 \text{ deg}$$

$$\theta_m = 10.4 \text{ deg}$$

$$L_1 = 441.11 \text{ in. (11.204 m)}$$

$$L_2 = 108.01 \text{ in. (2.743 m)}.$$

The focal length of M2 is equal to 260 in. (6.6 m). The exact dimensions are somewhat arbitrary but are constrained by limiting the M2 mirror projected diameter to 8 ft. (2.438 m); the larger the diameter, the higher the reflector above the elevation structure. The tube diameter was chosen such that the tube effects at S-band would be small [3]. It was subsequently necessary to design a feed system that provides a  $-18$  to  $-20$  dB taper at  $8.7$  deg (the illumination of the subreflector) and minimal spillover past  $10.4$  deg (the illumination of the BWG mirror).

Another important design parameter is the feed flare angle. Figure 7-8 shows the patterns and efficiencies (spillover times phase efficiency) for several different feed-horn flare angles. As can be seen, the patterns are not very sensitive to the flare angle. Since this was the case and the Jet Propulsion Laboratory (JPL) standard feed horn (designed for the DSN) has a flare angle of  $6.25417$  deg, it was decided to retain the standard flare angle in order to use existing feed horns and feed-horn designs.

Various feed-horn sizes with the JPL standard design angle of  $6.25417$  deg and frequency of  $8.45$  GHz were investigated. The goal was to find a horn with a  $-18$ -dB taper at  $\theta = 8.7$  deg (at subreflector distance,  $r = 425$  in. [10.8 m]) and a  $-23$ -dB taper at  $\theta = 10.4$  deg (at the parabolic mirror distance,  $r = 260$  in. [6.6 m]). The distances 6.6 m and 10.8 m are for a high-gain horn illuminating the BWG mirror M2 and the subreflector, respectively. The peak of the combined phase and spillover efficiencies ( $\eta_{\text{phase}} \times \eta_{\text{spill}}$ ) should optimally be between  $8.7$  deg to  $10.4$  deg. The results from various trials show that a 19-in. (48-cm) aperture diameter meets these goals. Figures 7-9 and 7-10 show amplitude, phase, and efficiency plots of the 19-in. X-band aperture diameter at  $r = 260$  in. and  $425$  in., respectively. From Fig. 7-9, the edge taper at the rim of the subreflector ( $\theta = 8.7$  deg,  $r = 425$  in.) is equal to  $-18.7$  dB, which is within

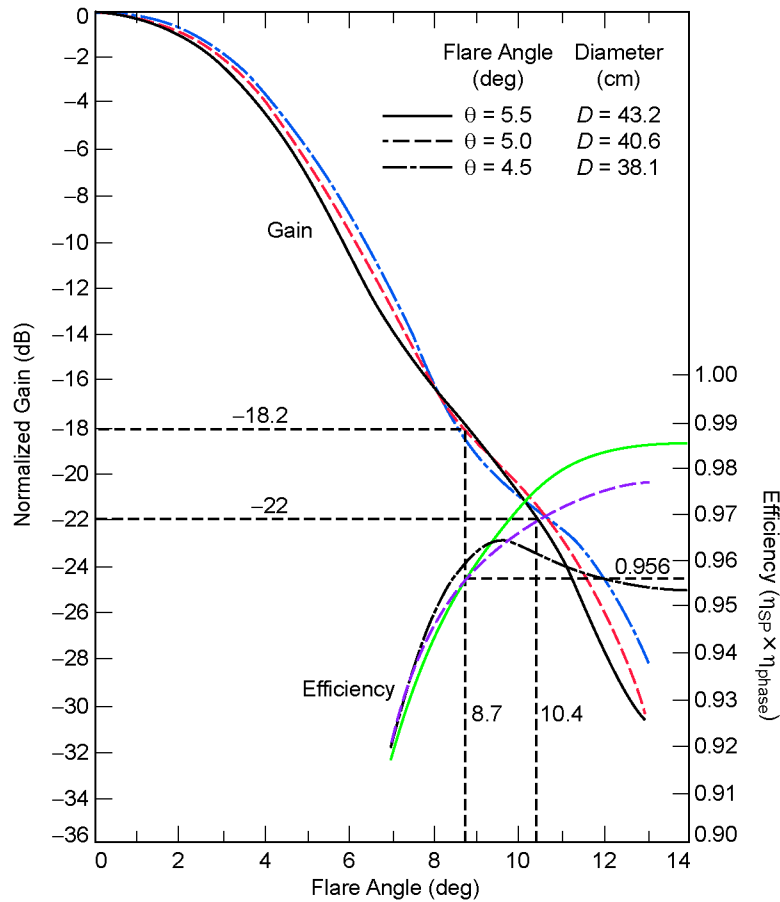


Fig. 7-8. Gain and efficiency versus flare angle.

the desired values of  $-18$  dB to  $-20$  dB. The combined phase and spillover efficiency is about 96.4 percent, where the maximum efficiency is about 97.8 percent at  $\theta \sim 11.5$  deg. This is a typical design point for a DSN antenna, since to use the maximum efficiency point usually results in a slightly larger subreflector. The results for a 20.8-in. (53-cm) aperture were very similar to those for the 48-cm aperture, but the 20.8-in. aperture results in a feed horn 11 in. (28 cm) longer at X-band; hence, the smaller design was chosen.

From Fig. 7-10, the edge taper at the rim of a BWG mirror (at  $r = 260$  in. [6.6 m]) is about  $-23.6$  dB at  $\theta = 10.4$  deg, with 96.5 percent efficiency. The maximum efficiency is equal to 96.7 percent at  $\theta = 9.8$  deg, which is desirable because the value falls between 8.7 deg and 10.4 deg. It was concluded that the 48-cm X-band horn had radio frequency (RF) radiation characteristics that met

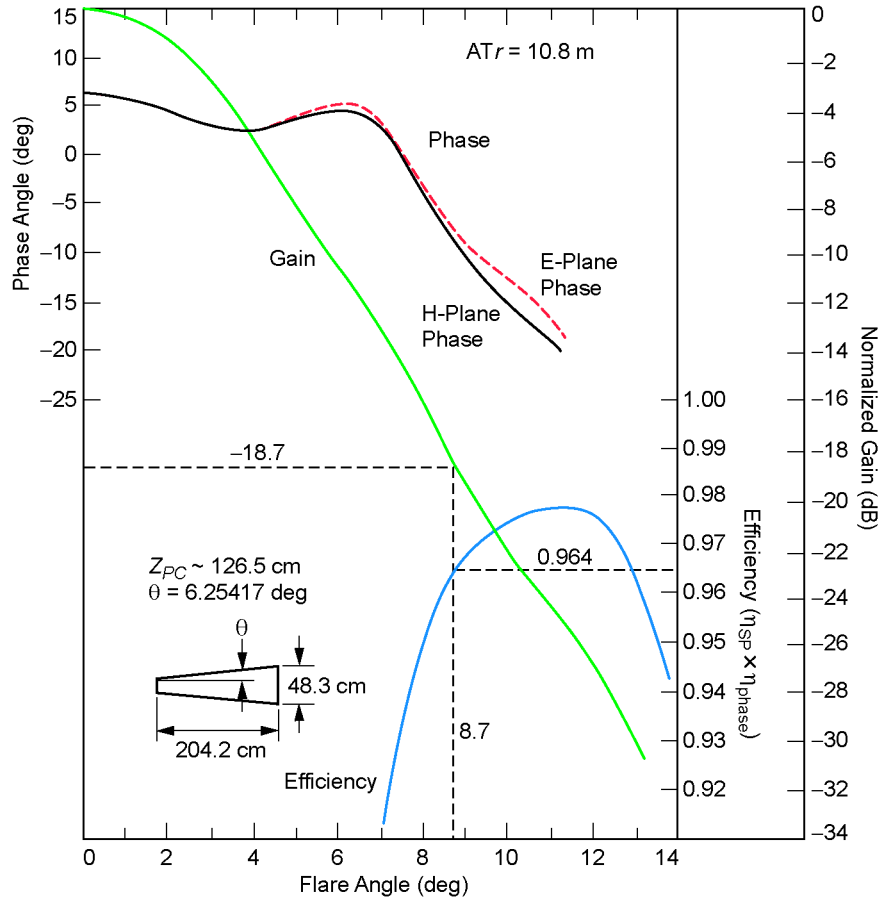


Fig. 7-9. Horn radiation pattern;  $R = 10.8$  m.

the requirements, and it was used in the design of BWG mirrors and the dual-shaped synthesis of the main and subreflector.

The choice of two identical paraboloidal sections for M2 and M3 has the following advantages:

- In the GO limit, a circularly symmetric input pattern still retains the original symmetric shape after reflection through both curved surfaces
- Since there is no caustic between the two curved mirrors, as there would be with ellipsoids, RF performance is not sensitive to the spacing ( $L_3$ ) between the two mirrors, provided that the spillover loss remains small
- A highpass-type RF performance is obtained with very good X-band performance for 8-ft (2.438-m) mirrors ( $<0.1$ -dB loss for this path) and optimum performance for Ka-band

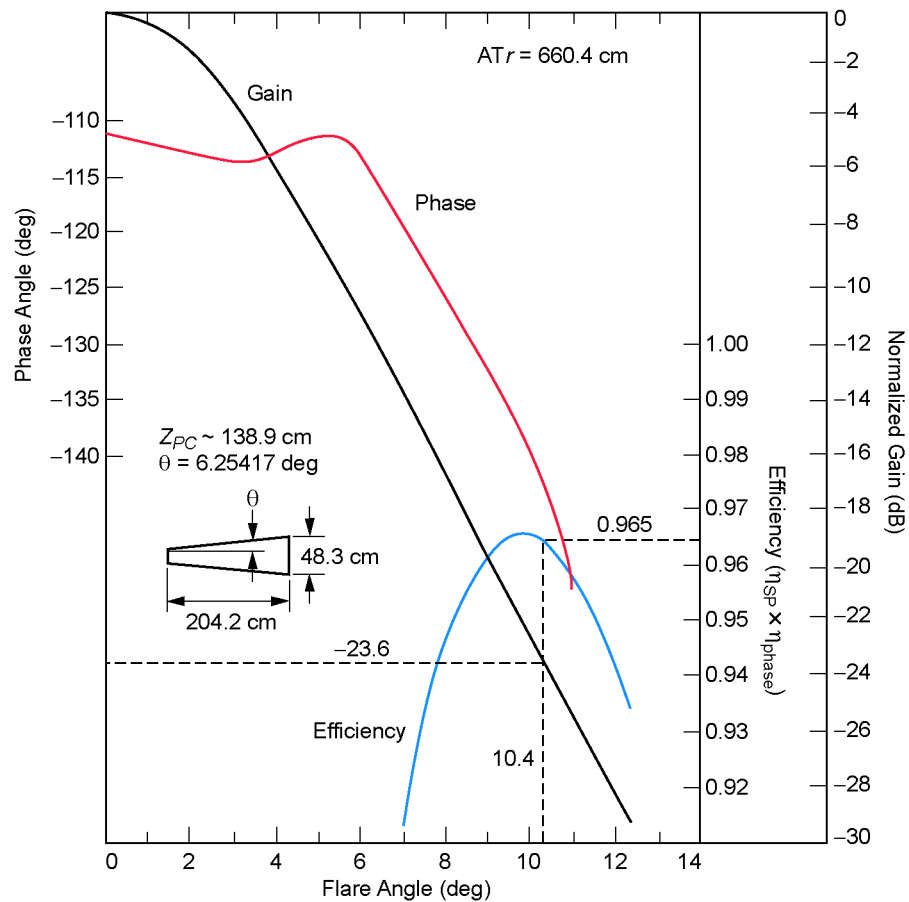


Fig. 7-10. Horn radiation pattern;  $R = 6.6$  m.

- When paraboloidal surfaces are used in the design, it is possible to have four identical mirrors (two for center-fed BWGs and two for bypass BWGs)
- Identical mirrors are more economical.

The centerline (CL) BWG paraboloidal mirrors are positioned so that feed horns and instrumentation packages can be either in an alidade location (not presently planned for implementation) or the pedestal room. Spacing between the two paraboloids,  $L_3 = 360$  in. (9.14 m), is chosen to allow enough head-room for vertical orientation of S-, X-, and Ka-band amplifier subassemblies. Also, S-band spillover loss at this distance is acceptably small. A flat plate, M4, reflects the RF beam downward, along the antenna azimuth axis, to the pedestal room, with focal point  $F_2$  about 79 in. (2 m) above the azimuth floor and about 197 in. (5 m) above the pedestal room ceiling.

A significant decision was whether to locate the feeds on the alidade at focal point  $F_2$  (requiring 29-dBi-gain feeds) or in the pedestal room, under the antenna, using focal point  $F_3$ . Despite an additional RF loss going from  $F_2$  to  $F_3$ , the clear advantages of using the pedestal room (more available space, no cable wrap across the azimuth axis, smaller feeds required, etc.) led to its selection. The stable environment of the pedestal room was a major design determinant.

### 7.3.3 Pedestal Room Optics Design

Only X- and Ka-bands were planned for Phase I operation of DSS-13. However, the design was required to have capabilities for future S-/X-, X-/Ka-, C-, and Ku-band operations (S-band is 2 GHz, C-band is 4–6 GHz, and Ku-band is 13–15 GHz). Low-gain horns (~22 dBi) are desirable for all frequency bands. A basic layout for the RF design in the pedestal room is given in Fig. 7-11. Mirror M5 is an ellipsoidal surface used for magnifying gain (reducing beamwidth) from 22 to 29 dBi and switching among various feed horns by rotating M5 about the antenna azimuth. Mirror M6 is a flat plate used to reflect the RF beam from a vertically positioned feed horn to M5, with angle  $\theta = 60$

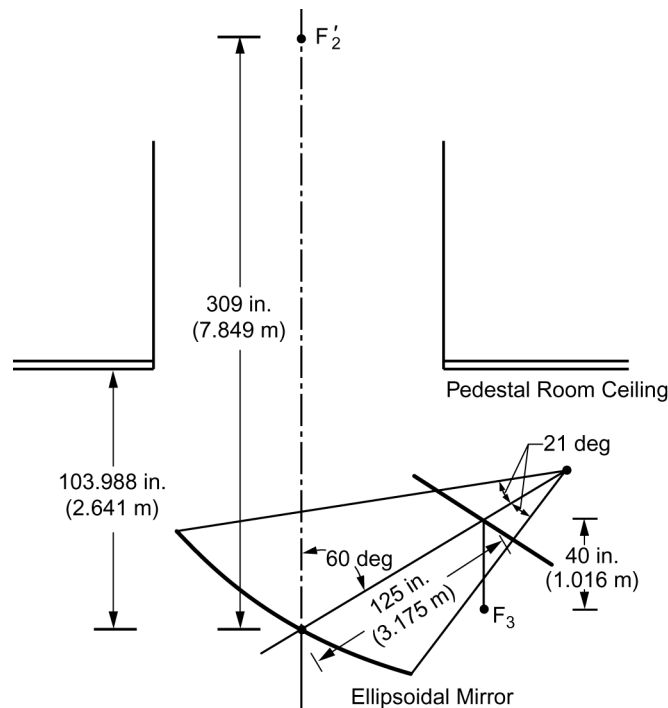


Fig. 7-11. Pedestal room geometry.  $F_3$  and  $F_2$  are the foci of the ellipsoid.

deg. The 60-deg angle is preferred because the existing JPL dichroic plate is designed with a 30-deg incident angle (equivalent to  $\theta = 60$  deg). Therefore, the  $\theta = 60$ -deg angle will be convenient for simultaneous operation (S-/X- and X-/Ka-band). Even though a smaller angle of  $\theta$  would yield a more symmetric beam pattern, angles smaller than 50 deg will have shadowing problems among M5, M6, and the feed horn. The curvature of M5 is determined by placing the near-field phase center of the 22-dBi X-band horn at a focal point of M5 ( $F_3$ ) and calculating the field at M3 by using PO. Iteration continues by changing the surface curvature of M5 until the scattered field has an average edge taper at M3 of about -23 dB. The mirror M5 is adjusted vertically until the best-fit phase center of the scattered field of M5 overlays  $F_2$ . The curvature and position of M5 are designed at X-band, and there is no vertical adjustment of the mirror for other bands. There is a vertical offset of 22.9 cm (9 in.) between the output GO focal point of M5 and the input GO focal point of M3. The Ka-band horn (or other high-frequency horns) must be defocused and the gain increased slightly (from 22 to 23 dBi) to approximate the same edge taper and best-fit phase center as at X-band. The detailed RF design layouts in the pedestal room for X- and Ka-bands are shown in Figs. 7-12 and 7-13. There are small lateral translations of the feed horns to compensate for radiation pattern asymmetry due to the surface curvature of mirror M5.

### 7.3.4 Bypass Beam-Waveguide Design

A layout of the bypass BWG is shown in Fig. 7-14. All mirrors rotate in azimuth and all in the elevation plane except M10. To allow enough clearance between mirror M10 and the elevation bearing, the bypass BWG vertical tube is positioned about ~403 in. (10.2 m) from the antenna centerline. The flat plate, M7, is removed when the center-fed BWG mode is used. Mirrors M8 and M9 are paraboloidal surfaces positioned to satisfy Mizusawa's conditions. Mirrors M7, M8, and M9 are attached to, and move together with, the main reflector structure. A flat mirror, M10, is attached to an elevation bearing; it is not rotated with elevation rotation (but moves with azimuth rotation) in order to have a focal point  $F_4$  always pointing straight downward to the alidade platform. By carefully adjusting  $L_5$  and  $L_6$  so that the distance from  $F_1$  to the mirror M8 is equal to 260 in. (660.4 cm), the paraboloidal mirrors M8 and M9 are identical to the mirrors M2 and M3 in the center-fed BWG design. Thus, there are four identical curved mirrors in this double BWG feed system.

The value of  $L_5$  used in this design is 290.645 in. (738.2 cm), which is the same as the spacing between mirrors M8 and M9. There is also enough clearance between an incident ray at the lower rim of M8 and the rim of the opening hole on the surface of the main reflector. Observe that the bypass performs slightly better than the center BWG, due to the absence of the ellipsoidal mag-

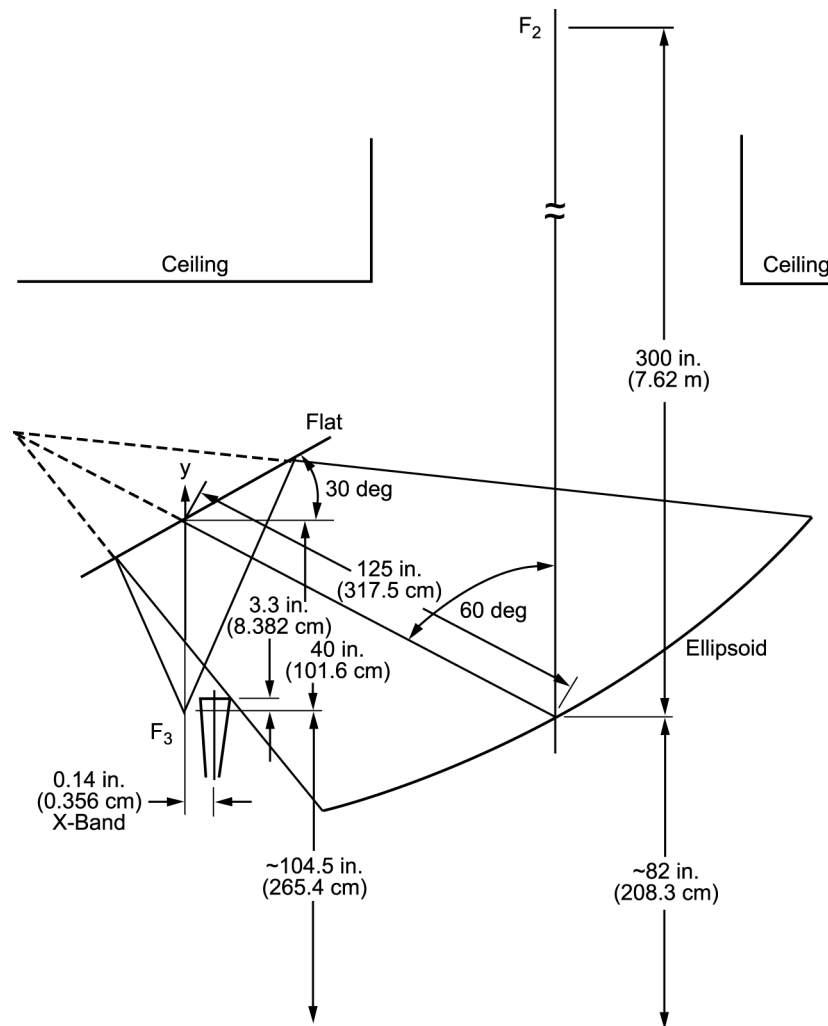


Fig. 7-12. Pedestal feed system for X-band.

nifier mirror and the shorter main path (290 in. versus 360 in. [736.6 cm versus 914.4 cm]).

### 7.3.5 Theoretical Performance

The theoretical performance of the BWG system is determined by using various combinations of analytical software, as described in [6] and [10]. Figure 7-15 shows the measured pattern of the input of the X-band 22-dBi horn fed at  $F_3$ , the calculated output of the ellipsoid at  $F_2$ , and demonstrates the X-band gain-magnifying (beamwidth-reducing) property of the ellipsoid.



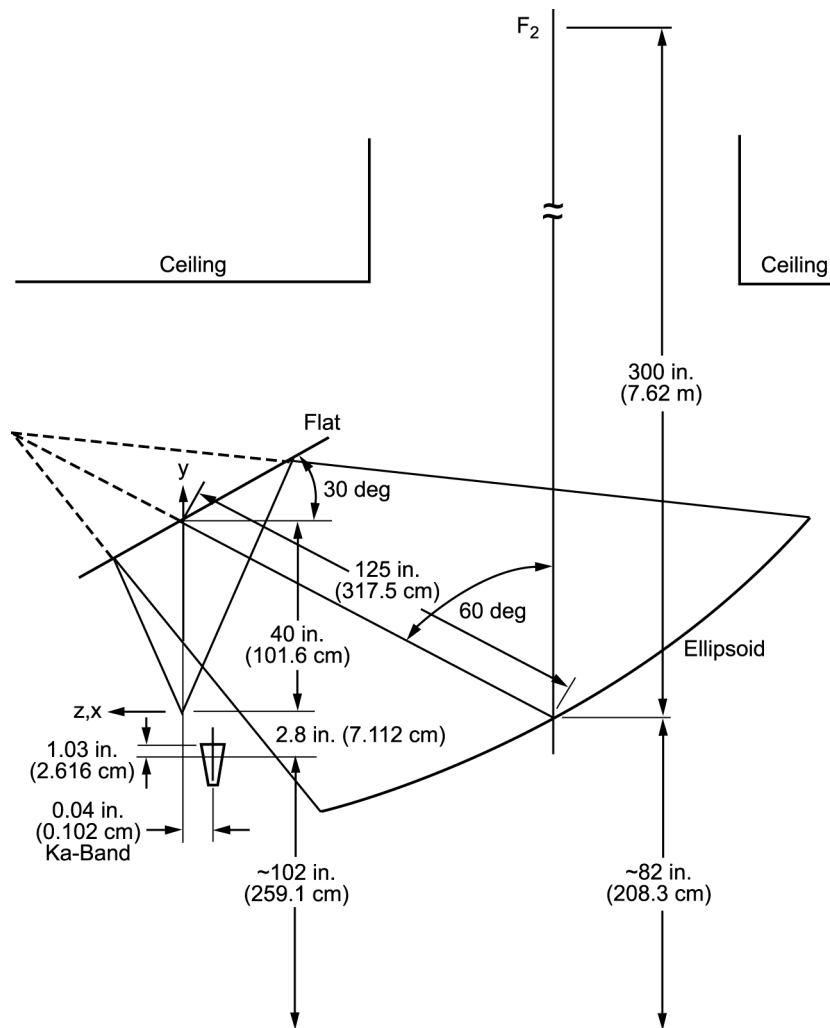


**Fig. 7-13. Pedestal feed system for Ka-band.**

Figure 7-16 shows the X-band output of the BWG at  $F_1$  compared with both the calculated input at  $F_2$  and the measured 29-dBi feed horn. Figure 7-17 shows a comparison of the E- and H-planes of the BWG output. The system is designed to image the 29-dBi horn at the input to the dual-reflector system. Figure 7-18 shows the input and output of the BWG at Ka-band and illustrates the nearly perfect imaging properties of the paraboloid pair. Figure 7-19 is a comparison of the 29-dBi feed horn located at  $F_1$  and the BWG feed horn located at  $F_3$  for the dual-reflector system at X-band.

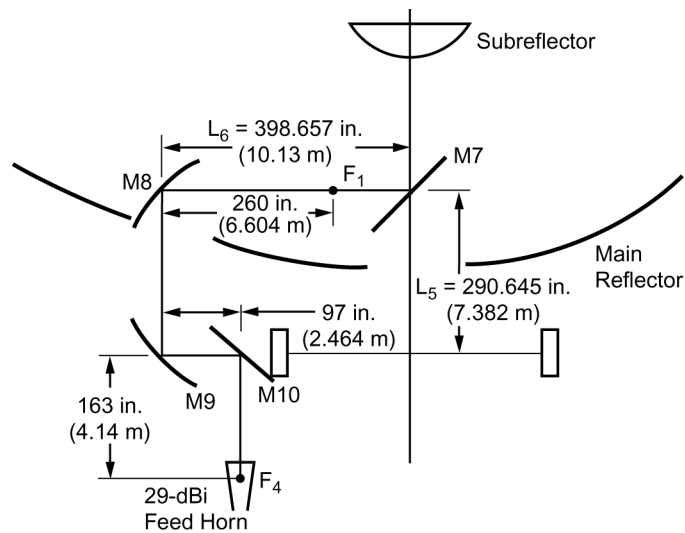


**Fig. 7-14. Details of the dimensions of the bypass beam-waveguide geometry.**

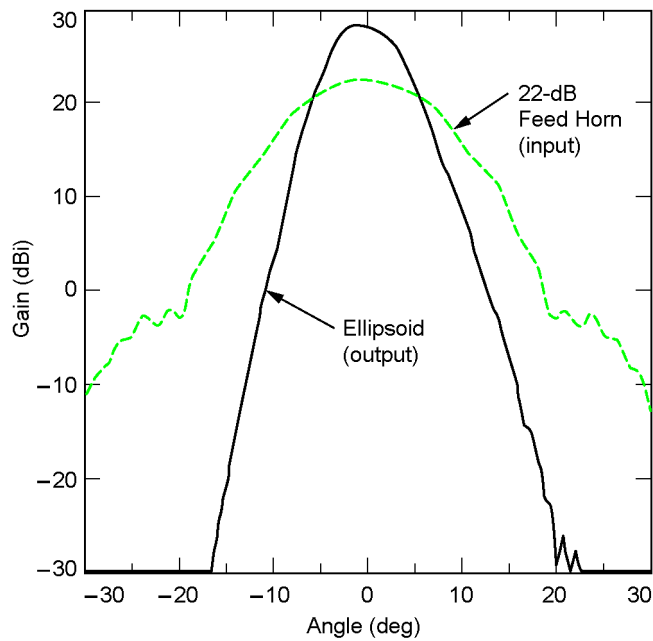


**Fig. 7-15. Beam-magnifier ellipse.**

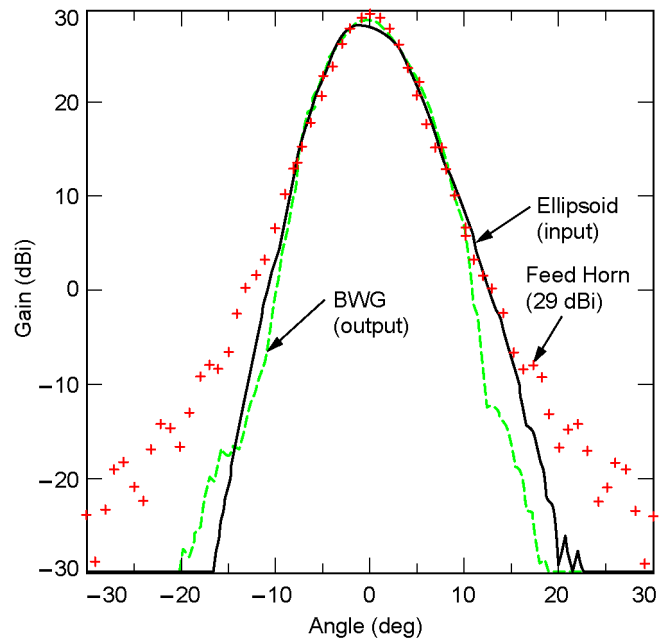


**Fig. 7-16. Center-fed output beam waveguide.**

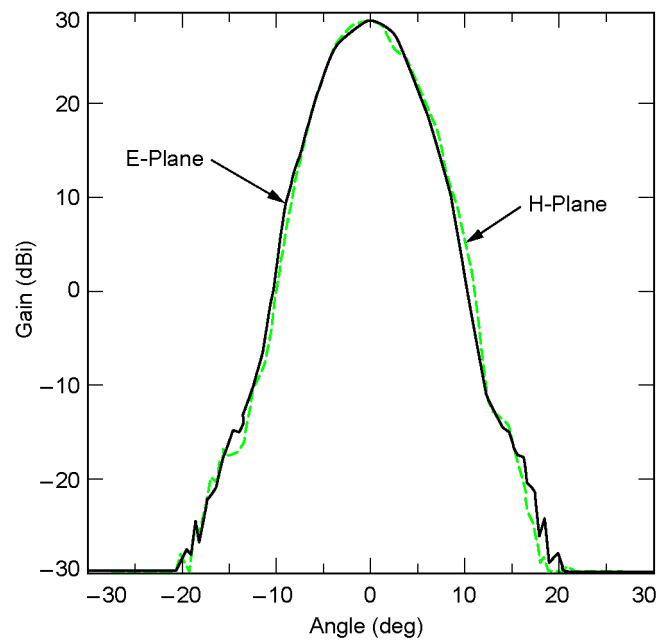


**Fig. 7-17. X-band E- and H-plane beam-waveguide output**

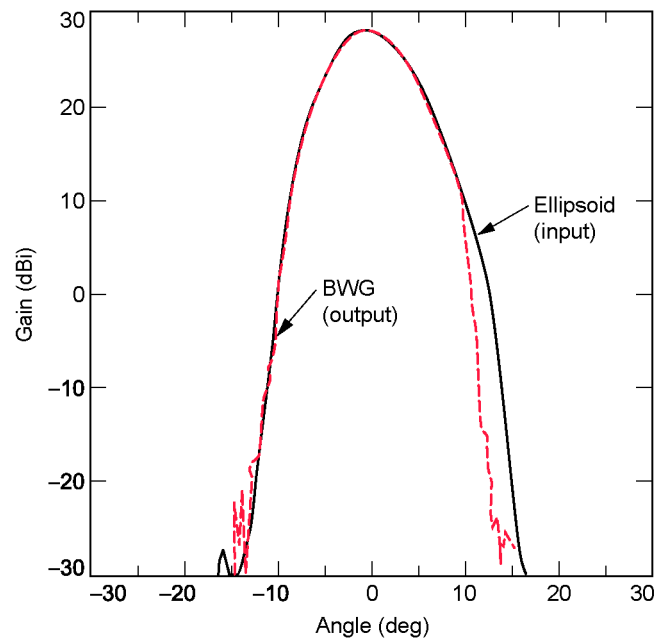


**Fig. 7-18. Ka-band center-fed beam-waveguide output.**

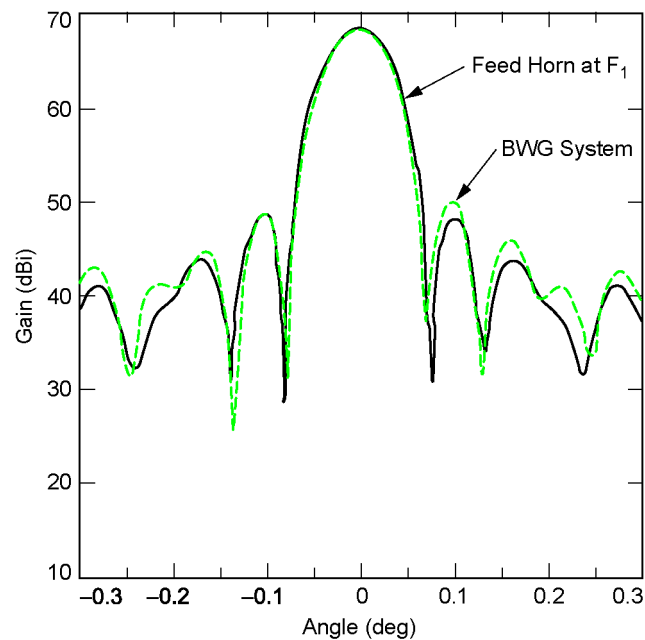


**Fig. 7-19. Comparison of horn versus beam-waveguide feeding the dual-reflector system.**

Table 7-1 lists the BWG losses at X- and Ka-band for both BWG systems and shows the reference HEF performance. The loss due to spillover was calculated with the assumption that the mirrors are in free space and that the energy not impinging on the mirrors is lost.

**Table 7-1. Beam-waveguide performance. (Losses due to surface rms, BWG mirror misalignments, subreflector support blockage, and feed system ohmic loss are not included.)**

Frequency (GHz)	Gain (dBi) (100% Efficient)	DSS-15 HEF Cassegrain	DSS-13 Bypass BWG		DSS-13 Center-Fed BWG		
		Gain (dBi)	Gain (dBi)	Portion Due to Spillover	Gain (dBi)	Paraboloid Spill Portion	Ellipsoid Spill Portion
8.45 (X-band)	69.57	69.21	69.13	−0.06	69.06	−0.06	−0.06
31.4 (Ka-band)	80.98	80.62	80.55	−0.06	80.42	−0.03	−0.03

### 7.3.6 Dual-Shaped Reflector Design

The requirement for dual-shaped reflectors is to design the contour of the main reflector surface to be within  $\pm 0.5$  in. ( $\pm 1.2$  cm) of the contour of the HEF antenna. The reason for this is to be able to use the existing backup structure together with the new panels.

The X-band feed-horn pattern at  $r = 425$  in. (10.8 m) (the mean distance to the subreflector) is used as an input pattern to the synthesis program developed by Galindo [11]. The basic input parameters were similar to those of the HEF antenna design. The maximum difference between the main reflector surfaces of DSS-13 and those of the HEF antenna is 1.1 cm, which is below the 0.5-in. (1.2-cm) requirement. The corresponding rms is only 0.2 mm, which means the two contours are very close to each other over most of the surface of the dish.

### 7.3.7 The Effect of Using the DSS-15 Main Reflector Panel Molds for Fabricating DSS-13 Panels

In 1988, when the DSS-13 BWG antenna project was still in the planning stages, it was decided that to reduce costs, the main reflector panels for the DSS-13 antenna should be made from the available molds that were used to make the main reflector panels for the DSS-15 antenna. For both antennas, the

main reflector surface is made up of nine rings of panels (see Fig. 7-20), with all panels in a given ring identical in shape. The differences in the shape of the panels for the two antennas were minor, and it was believed they would not significantly affect the required performance of the new R&D antenna.

Looking at each of the nine panel rings individually and assuming that the panels on the DSS-13 antenna were made accurately from the DSS-15 manufacturing contours, the panels were mathematically best-fitted to the DSS-13 design contour. The axial errors between these two contours were calculated for each of the nine panel rings by subtracting the reference DSS-13 required shape from the DSS-15 panel contour.

The errors in the first seven panel rings for DSS-13 are minor and cause no significant performance loss at 32 GHz. The errors in panels 8 and 9 are much more significant and contribute noticeably to RF performance degradation at 32 GHz. (It should be noted that the outer half of panel 9 is a noise shield and should not be viewed as contributing to RF gain performance.)

Figures 7-21 and 7-22 show the holographically derived surface errors for rings 8 and 9, respectively, overlaid on the predicted mechanical surface errors for these panels. These plots show good agreement between the manufacturing contour and the holography measurements.

The current antenna surface has an error of 0.28 mm for the inner seven panel rings, 0.60 mm for rings 8 and 9 together, and 0.40 mm for all of the antenna, excluding the noise shield.

The errors in the DSS-13 BWG antenna surface in the outer two panel rings have been measured accurately and are noticeable in 32-GHz performance.

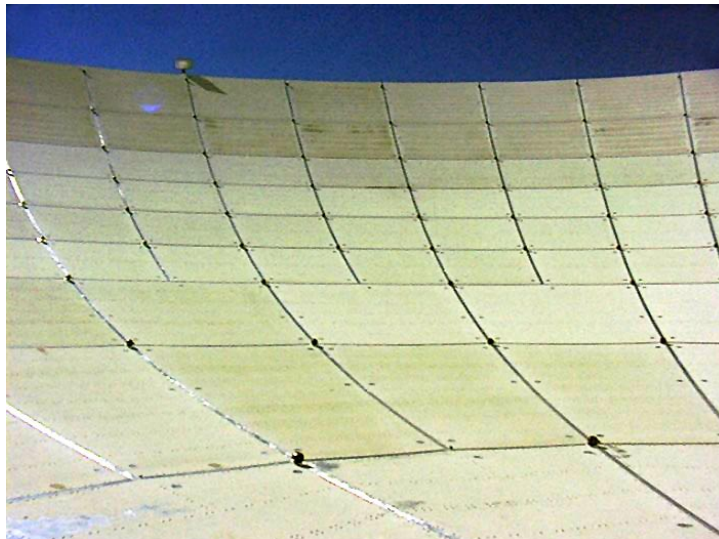


**Fig. 7-20. The 34-m antenna main reflector panel rings.**

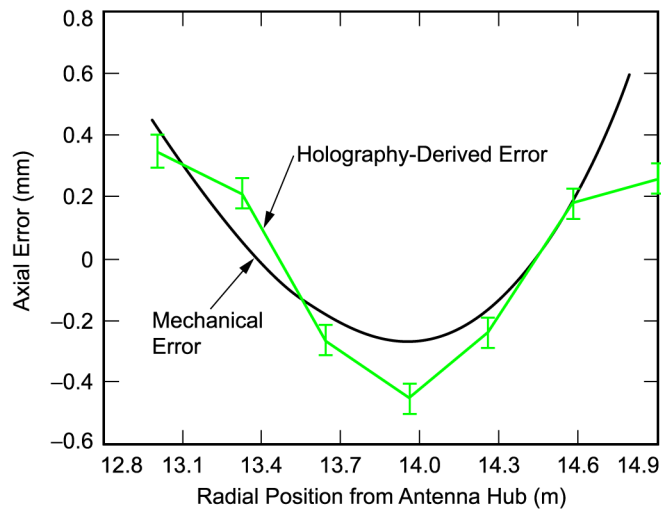


**Fig. 7-21. Mechanical error in panel ring 8, with holographically derived average phase-error function.**

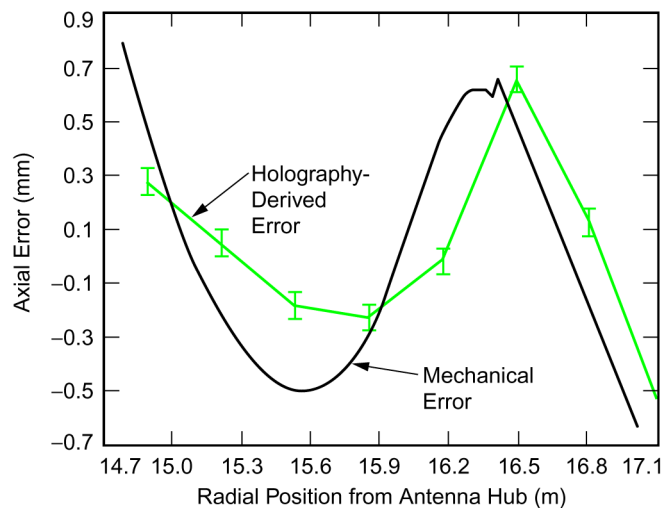


**Fig. 7-22. Mechanical error in panel ring 8, with holographically derived average phase-error function.**

Estimates have been made as to the possible gain improvement that would be obtained if these panels were replaced by panels that had surface errors on the order of those seen on the inner seven panel rings. The outer two rings incorporate 37 percent of the aperture area, not including the noise shield. If this area

of the antenna were to have its rms error decreased from 0.60 mm to 0.28 mm, the increase in antenna gain would be 0.6 dB at 32 GHz. The present Ka-band area efficiency of 52 percent at  $F_1$  would increase to 60 percent.

## 7.4 Phase I Measured Results

The testing method used on the BWG antenna is unique in that a direct experimental measurement can be made of the degradation contributed by the BWG mirror system. The methodology is to use a portable test package that can be transported to focal point locations  $F_1$ ,  $F_2$ , and  $F_3$ . The phase center of the feed horn on the portable test package is made to coincide with the desired focal points, for example,  $F_1$ . Measurements are made of system temperatures and antenna efficiencies at  $F_1$ . The differences between system temperatures at  $F_1$  and those on the ground give a measure of the additional contributions due to tripod scattering, main reflector spillover, and leakage. The test package is then taken to one of the other focal points ( $F_2$  or  $F_3$ ) and measurements are again made of system temperatures and efficiencies. The differences in measurements give a direct measure of the degradations caused by the BWG system mirror and surrounding shrouds. To the author's knowledge, this is the first use of a portable test package to test the integrity of a BWG antenna.

### 7.4.1 The X- and Ka-Band Test Packages

Figure 7-23 shows the system block diagram of the X-band test package [12]. Depicted are the usual Cassegrain front-end components such as a 22-dBi feed horn, polarizer, round-to-rectangular waveguide transition, waveguide switch, cryogenically cooled low-noise amplifier (LNA), and downconverter. The LNA is a high-electron-mobility-transistor (HEMT) assembly described in [13]. Noise-temperature calibrations are performed with the incorporation of a remotely controlled noise-diode assembly and a digital-readout thermometer embedded in an ambient-load-reference termination. For the X-band test package, the microwave signal is downconverted to 350 MHz and sent via coaxial cable to a total-power radiometer (TPR) system.

In order to test the antenna at  $F_1$  and  $F_3$ , the test package is required to be convertible from 29-dBi to 22-dBi feed-horn configurations. This is accomplished through the removal of horn extensions of the same taper going from aperture diameters of about 19 to 7.08 in. (48 to 18 cm).

Figure 7-24 is a photograph of the fabricated and assembled X-band test package in its 22-dBi feed-horn configuration for testing the system on the ground. The test package is about 94.5 in. (2.4 m) high in the 22-dBi horn configuration.



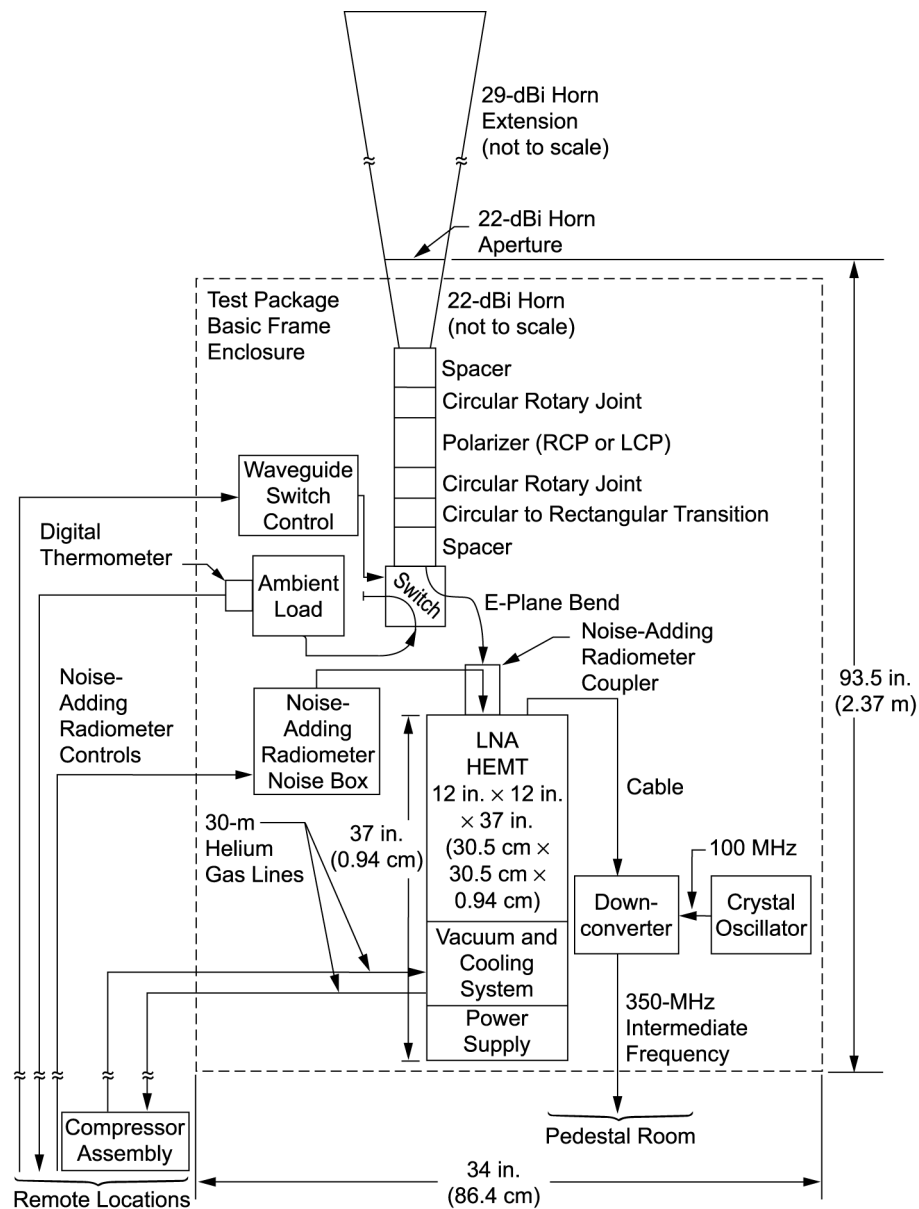


Fig. 7-23. Block diagram of the X-band test package system.

The Ka-band test package design is very similar to that of the X-band package and is described in [14].



**Fig. 7-24. X-band test package in the 22-dBi feed-horn configuration for testing.**

#### **7.4.2 Noise Temperature**

Figure 7-25 shows the portable X-band front-end test package with the 29-dBi horn installed on the antenna at  $F_1$  [15]. A tape measure indicated that the desired and actual horn phase-center locations agreed to within 0.25 to 0.12 in. (6.3 to 3.1 mm), with measurements accurate to  $\pm 0.06$  in. ( $\pm 1.5$  mm). After completion of the noise-temperature and antenna-efficiency measurements at  $F_1$ , the X-band test package was removed and reconfigured to a 22-dBi feed-horn configuration, and installed at  $F_3$  (Fig. 7-26). The mounting table shown in Fig. 7-26 is a universal mount that can support any of the test packages and provide three-axis adjustment of the test-package location. The summary of the X-band zenith system temperatures at DSS-13, from June 10, 1990, to February 2, 1991, is shown in Table 7-2. The differential zenith system temperatures for the various test configurations are shown in Table 7-3. Observe that the degradation in noise temperature for the BWG antenna using the 22-dBi feed horn was 8.9 K. This is significantly higher than originally expected.

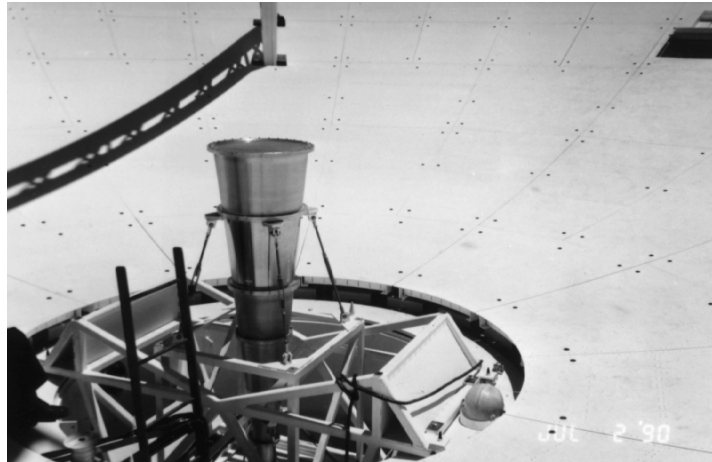


**Fig. 7-25. X-band 29-dBi feed-horn test package and mounting assembly installed at  $F_1$ .**

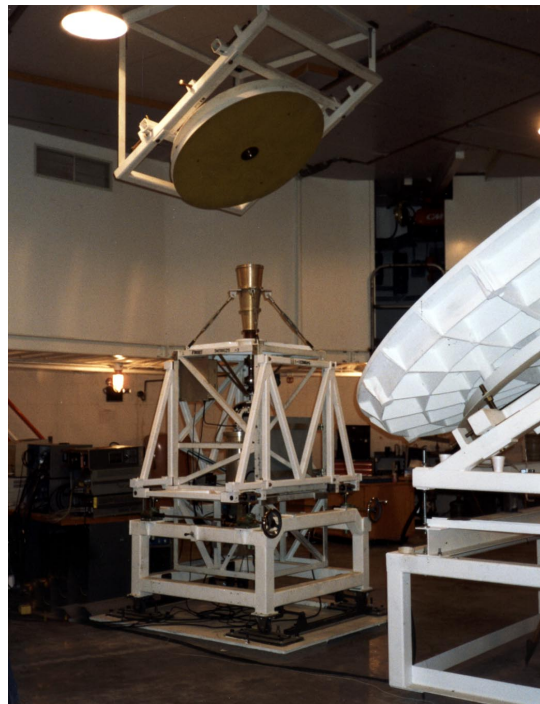


**Fig. 7-26. X-band 22-dBi feed-horn test package and mounting table installed at  $F_3$ .**

**Table 7-2. Summary of X-band zenith operating-system temperatures at DSS-13 from June 10, 1990, to February 2, 1991.**

Configuration	Observation Dates	Grand Average <sup>a</sup> $T_{op}$ (K)	Peak Deviations from Grand Average (K)
Ground	06/10/90 01/21/91 01/26/91	22.7	+0.3
F <sub>1</sub>	10/04/90	25.9	Not available
F <sub>3</sub>	11/06/90 11/09/90	34.2	+0.1/−0.1
After mirrors and ellipsoid were realigned on December 18, 1990			
F <sub>3</sub>	01/31/91 02/02/91	34.8	+0.1/−0.1

<sup>a</sup>See Table 5 in [15] for the average  $T_{op}$  (system-noise temperature) for each observation period. These values formed the basis for obtaining the grand average for a particular test configuration.

**Table 7-3. Differential zenith operating-system temperatures for various test configurations at 8.45 GHz.**

Configurations Differenced <sup>a</sup>	Delta $T_{op}$ (K)
F <sub>1</sub> – ground	3.2
F <sub>3</sub> – F <sub>1</sub>	8.3
After mirrors and ellipsoid were realigned on December 18, 1990	
F <sub>3</sub> – F <sub>1</sub>	8.9

<sup>a</sup>See Table 7-2 for ground, F<sub>1</sub>, and F<sub>3</sub> values.

The Ka-band 29-dBi feed-horn test package [14] was installed on the antenna at the Cassegrain focal point F<sub>1</sub>, and measurements were made of noise temperature and efficiency. After completing the measurements at F<sub>1</sub>, the Ka-band test package was removed and then modified to a 23-dBi horn configuration and installed at F<sub>3</sub> on the universal mounting assembly [16]. The noise-temperature data is summarized in Tables 7-4 and 7-5. The degradation caused by the BWG system at Ka-band was 6.8 K.

**Table 7-4. Summary of Ka-band zenith operating-noise temperatures at DSS-13, from October 12, 1990, through January 31, 1991.**

Configuration	Observation Dates	Grand Average <sup>a</sup> $T_{op}$ (K)	Peak Deviations from Grand Average (K)
Ground	10/12/90, 11/09/90, 01/19/91, 01/31/91	84.7 <sup>b</sup>	+1.6/−1.7
F <sub>1</sub>	10/13/90, 10/14/90, 01/11/91	91.8	+0.4/−0.6
F <sub>2</sub>	01/16/91, 01/17/91	97.0 <sup>c</sup>	+0.4/−0.4
F <sub>3</sub>	11/10/90, 12/18/90	102.4	+0.1/−0.0
After mirrors and ellipsoid were realigned on December 18, 1990			
F <sub>3</sub>	01/23/91, 01/25/91, 01/30/91	98.6 <sup>d</sup>	+0.1/−0.1

<sup>a</sup> See Table 3 in [16] for the average  $T_{op}$  for each observation period. These values formed the basis for obtaining the grand average for a particular test configuration.

<sup>b</sup> Ground values were reported in Part I of [14]. The measured ground value of 84.7 K agrees closely with the predicted value of 84.5 K under standard conditions.

<sup>c</sup> No calibrations longer than 10 min were done at F<sub>2</sub> with the antenna left at zenith.

<sup>d</sup> This number cannot be compared with the above F<sub>2</sub> value. It is probable that the new F<sub>2</sub> value was also lower after the mirror realignment, but a measurement was not made.

**Table 7-5. Differential zenith operating-noise temperatures for various test configurations at 32 GHz. (See Table 7-4 for F<sub>1</sub>, F<sub>2</sub>, and F<sub>3</sub> values. Do not compare the values for F<sub>3</sub> − F<sub>1</sub> after December 18, 1990, with the value for F<sub>2</sub> − F<sub>1</sub> because the value at F<sub>2</sub> might have become lower, but was not remeasured.**

Configurations Differenced	Delta $T_{op}$ (K)
F <sub>1</sub> − ground	7.1
F <sub>2</sub> − F <sub>1</sub>	5.2
F <sub>3</sub> − F <sub>1</sub>	10.6
After mirrors and ellipsoid realigned on December 18, 1990	
F <sub>3</sub> − F <sub>1</sub>	6.8

### 7.4.3 Efficiency Calibration at 8.45 and 32 GHz

From July 1990 through January 1991, the 34-m-diameter BWG antenna at the NASA Goldstone deep space communications complex in California's Mojave Desert was tested as part of its postconstruction performance evaluation [17].

Efficiency and pointing performance were characterized at 8.45 and 32 GHz (X- and Ka-bands, respectively) at both the Cassegrain ( $F_1$ ) and BWG ( $F_3$ ) focal points. The  $F_1$  focal point is located close to the vertex of the main reflector while the  $F_3$  focal point is located about 35 m away, in a subterranean pedestal room.

Through the use of the X- and Ka-band portable test packages, located at both  $F_1$  and  $F_3$ , a direct experimental measurement was made of antenna efficiency and gain degradation caused by the BWG mirror system.

The measurement of antenna efficiency involves boresighting the antenna, measuring the increase in noise temperature due to a radio source of known flux density, and correcting for atmospheric attenuation and radio source size. The technique is well described in both Chapter 1 of this monograph and [17] and will not be repeated here.

The predicted gains at X-band were 68.54 dBi at  $F_1$  (the focus of the dual reflector system) and 68.29 dBi for  $F_3$  (the focal point of the BWG feed system). The measured efficiency and gain at 8.45 GHz were reported to be 0.754 and 68.34 dBi for  $F_1$  and 0.724 and 68.17 dBi for  $F_3$  [18]. Since the antenna had a significant main reflector surface distortion as a function of elevation angles, the Ka-band predictions are applicable only for a main reflector adjustment or rigging angle near 45-deg elevation. The predicted  $F_1$  total efficiency and overall gain were 0.527 and 78.36 dBi, respectively. The corresponding measured efficiency and gain were 0.523 and 78.33 dBi. At  $F_3$ , the predicted total antenna efficiency and overall gain at 32 GHz are, respectively, 0.452 and 77.70 dBi, as compared to the measured efficiency and gain values of 0.449 and 77.66 dBi. In general, the agreement between predicted and measured Ka-band efficiencies and gains was very good.

A summary of the X- and Ka-band measured points (adjusted for proper flux values) is shown in Fig. 7-27. The variation of Ka-band gain as a function of elevation angle is quite apparent.

The complete Phase I testing of the BWG antenna is summarized in [19].

### 7.4.4 Optimizing the G/T Ratio of the Beam-Waveguide Antenna

During Phase I testing of the DSS-13 BWG antenna, it was discovered that there was higher system-noise temperature than expected. The high noise temperature was caused by the spillover losses of the BWG mirrors having a greater effect than previously thought. It was experimentally determined that

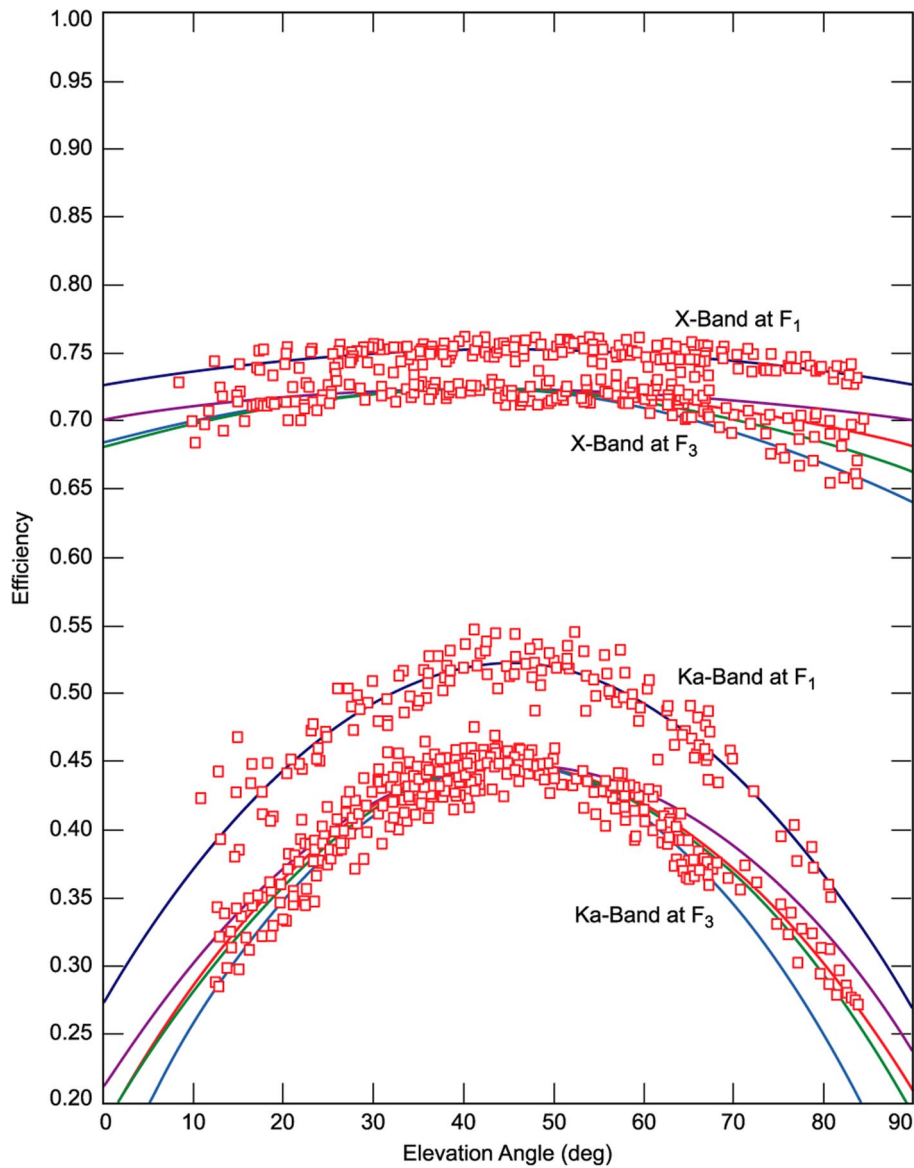


**Fig. 7-27. DSS-13 X- and Ka-band efficiencies at  $F_1$  and  $F_3$  focal points, without atmosphere.**

higher-gain feed horns would improve the  $G/T$  ratio of the antenna for two reasons: (a) there would be a lower spillover loss in the BWG mirrors and, hence, less noise temperature, and (b) when using higher-gain feed horns, the antenna gain would not decrease significantly.

With three different feed-horn patterns as inputs, the PO software was used to analyze the theoretical performance of the DSS-13 BWG antenna [20]. The three patterns used were those of corrugated horns with far-field gains of 22.5, 24.2, and 26.1 dB. Each horn pattern was placed at different positions along the  $z$ -axis from  $F_3$ , the focal point of the basement ellipsoid. From the PO analysis, the spillover of the BWG mirrors and the gain of the DSS-13 BWG antenna could be obtained and, in this manner, various  $G/T$  values could be calculated. All of these calculations were done at 8.45 GHz.

The theoretical feed-horn patterns were modeled using the corrugated horn program described in Chapter 1 of this monograph. The far-field horn patterns were then converted into a set of spherical-wave-expansion (SWE) coefficients and then input into the PO software to obtain the gain of the antenna and spillover of the BWG mirrors. The noise temperature was approximated by ignoring the effects of the BWG tubes and converting spillover energy into noise temperature, using an appropriate temperature factor for the particular mirrors. The technique is further described in [21]. The calculations are summarized in Fig. 7-28.

Figure 7-28(a) shows the efficiency of the DSS-13 BWG antenna for various feed horns as a function of the horn aperture position measured from  $F_3$ . The efficiency plotted in Fig. 7-28(a) includes the BWG spillover losses and the other losses associated with the antenna. For example, the PO software predicts a gain of 68.933 dB for the 22.5-dB corrugated horn with its aperture located  $2\lambda$  from  $F_3$ . This gain corresponds to an efficiency of 86.36 percent at  $f = 8.45$  GHz (69.57 dB is equivalent to 100 percent). The 86.36 percent efficiency would then be multiplied by the efficiency that represents the other losses (84.6 percent) to give a total efficiency of 73 percent [see Fig. 7-28(a)]. This result agrees well with the reported measured value of 72.4 percent.

Figure 7-28(b) shows the total noise temperature of the DSS-13 BWG antenna due to the ultralow-noise amplifier (ULNA) and the feeds as a function of horn aperture position with respect to  $F_3$ . The ULNA [22] was an X-band ultralow-noise maser specifically designed to operate with the BWG antenna. The total noise temperature was obtained by adding the baseline temperature of 11.05 K of the ULNA to the contributions of the six BWG mirrors, the subreflector and the 34-m main reflector. As expected, the noise temperature decreased as higher-gain horns were used, because they caused less spillover in the BWG mirrors than the lower-gain horns.

For example, for the 22.5-dB corrugated feed horn with its aperture located  $2\lambda$  (7.1 cm) from  $F_3$ , the PO software predicts a spillover noise temperature of 9.41 K. This value is obtained by subtracting the amplifier noise temperature (11.05 K) from the value in Fig. 7-28(b) (20.46 K). This value was calculated by taking the spillovers computed by the PO software and modifying values, using the appropriate temperature factors. The measured BWG noise temperature



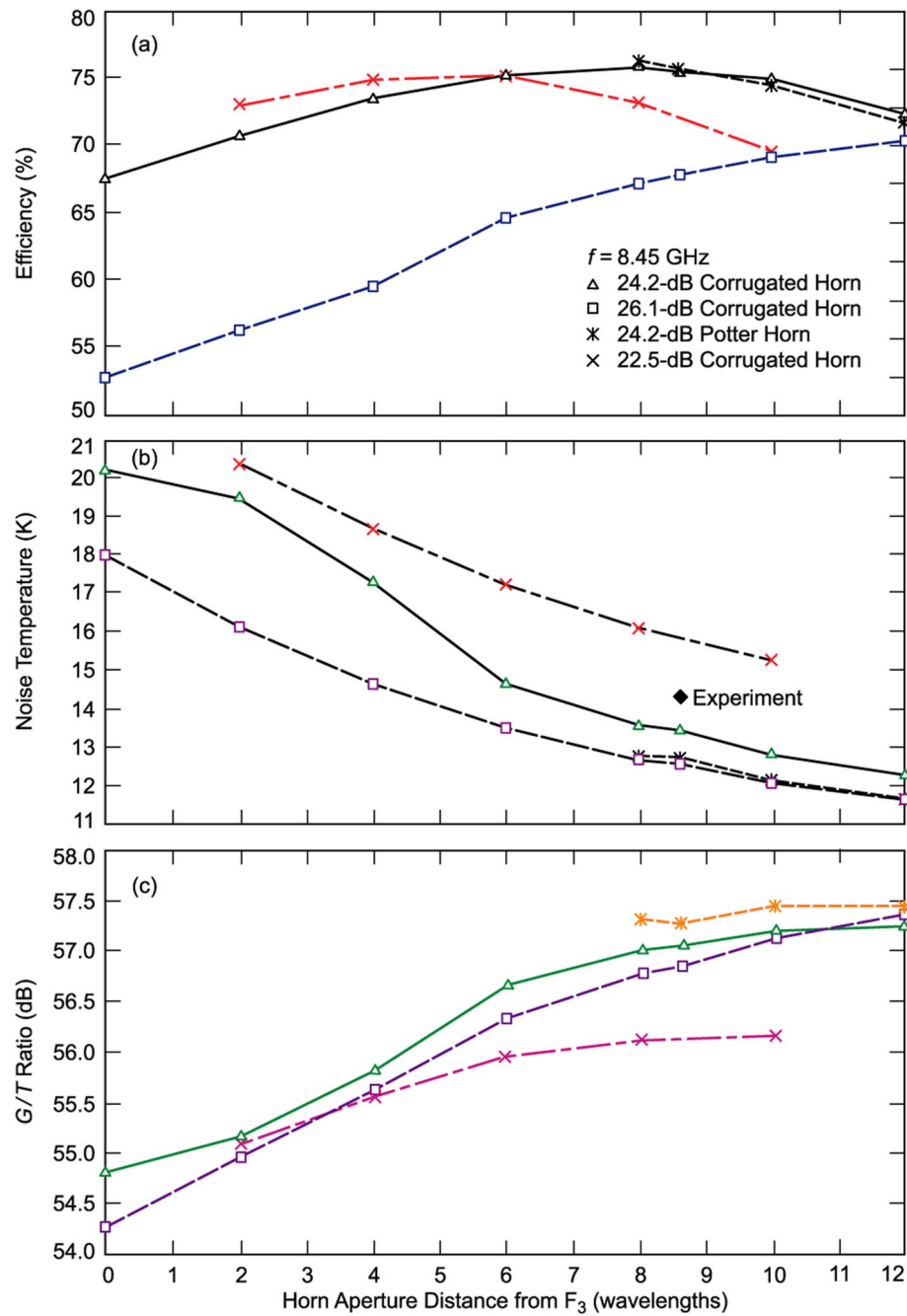


Fig. 7-28. DSS-13: (a) efficiency versus feed-horn aperture distance from  $F_3$ , (b) system temperature versus horn-aperture distance from  $F_3$ , and (c)  $G/T$  ratio versus horn-aperture distance from  $F_3$ .

using this horn was 8.9 K when the aperture was placed about 3.3 in. (8.4 cm) from  $F_3$ .

Figure 7-28(c) shows the  $G/T$  values of the DSS-13 BWG antenna for the horns as a function of their aperture position with respect to  $F_3$ . The  $G/T$  ratio is calculated by converting the efficiencies of Fig. 7-28(a) to decibels and then subtracting the total noise temperature (in decibels).

Observe that a feed-horn gain in the 24–26-dBi range gives the optimum  $G/T$ . It was desirable to verify the improved performance experimentally and, because of cost constraints, it was decided to use a smooth-wall Potter horn instead of a corrugated horn. A 24.2-dB Potter horn was chosen because it had been determined to have nearly the same spillover as the 26.1-dB corrugated horn.

The new 24.2-dB Potter feed horn was then run through the PO software as the other horns had been. The results are shown in Fig. 7-28. Only four cases were run for this horn because results for the corrugated horns predicted that the optimum  $G/T$  ratio would be achieved when the horn aperture-to- $F_3$  displacement was about  $10\lambda$ . Notice that the predicted  $G/T$  ratio for the 24.2-dB Potter horn is better than for all the horns. This is because while the antenna efficiency is at the same level as for the 24.2-dB corrugated horn [see Fig. 7-28(a)], the noise temperature is about 0.7 K lower [see Fig. 7-28(b)].

The new 24.2-dB Potter horn was built, and radiation patterns were measured. Then, in November 1991, the system-noise temperature of the DSS-13 BWG antenna was measured using the 24.2-dB Potter horn with the ULNA. The horn's aperture was placed  $8.61\lambda$  ( $f = 8.45$  GHz) from  $F_3$ . A value of  $N_i = 14.4$  K was observed. The measured point is shown in Fig. 7-28(b). The predicted noise temperature for the 24.2-dB Potter horn was 12.78 K.

#### 7.4.5 Beam-Waveguide Antenna Performance in the Bypass Mode

The 34-m BWG antenna was designed with two BWG receiver paths: a centerline feed system, which terminates in the pedestal room at the  $F_3$  focal point; and a bypass feed system, which terminates on the alidade structure at the  $F_4$  focal point (Fig. 7-6). The centerline feed system has already been evaluated for zenith operating-noise temperature and antenna-area efficiency performance at X-band (8.45 GHz) and Ka-band (32 GHz) at the two focal points,  $F_1$  and  $F_3$  [15–17]. The bypass BWG feed system has also been evaluated at both X-band and Ka-band [23]. In order to maintain consistency, the same test packages that were used to evaluate the centerline feed BWG system were used to test the bypass BWG feed system.

**7.4.5.1 X-Band Measurements.** The X-band test package with its 29-dBi feed horn was used to make comparative zenith operating-noise temperature

measurements at two locations: on the ground and on the antenna at the  $F_4$  focal point. Table 7-6 shows the compiled results of the X-band  $T_{op}$  (total system-noise temperature) measurements as well as the weather conditions present during the observation period. Table 7-6 also shows the corrections that were made to the operating-noise temperature measurements in order to normalize them to the weather conditions present during an average Goldstone day.

Normalizing the  $T_{op}$  measurements to a fixed weather condition, it is easier to compare these measurements with each other as well as with those made at any other time of the year. As a means of comparison between these results for  $F_4$  and the results obtained previously for  $F_1$  and  $F_3$ , Table 7-7 contains a summary of some differential zenith operating-noise temperatures. All of the  $T_{op}$  values presented in Table 7-7 have been normalized to standard DSS-13 atmospheric conditions at 8.45 GHz.

The antenna's efficiency performance was determined by continuously tracking a stellar radio source and measuring the peak received noise power in relation to the background atmospheric noise over a full 10- to 12-h track. By knowing the maximum signal strength of the radio source, the aperture efficiency with respect to the elevation angle of the antenna can be determined.

Figure 7-29 shows the combined antenna efficiency measurements at X-band versus elevation angle for the  $F_4$  focal point, with the effects of atmospheric attenuation removed. An average antenna efficiency with a peak of 71.4 percent at an elevation angle of 38.6 deg is also shown in this figure.

**7.4.5.2 Ka-Band Measurements.** As with X-band, the Ka-band test package with its 29-dBi feed horn was used to make comparative zenith  $T_{op}$  measurements on the ground and at the  $F_4$  focal point. Continuous measurements at each of these locations were made over two-day periods, with operating-noise-temperature measurements taken every 30 min and ambient weather conditions measured every 10 min. As with the X-band measurements described above, corrections for gain changes are already accounted for in the operating noise-temperature measurements, and no corrections were made for linearity, which would have an effect of less than  $\pm 2$  percent.

Table 7-6 shows the compiled results of the Ka-band  $T_{op}$  measurements, as well as the weather conditions present during the observation period. The normalized  $T_{op}$  values, which were calculated, are also included in this table.

Table 7-7 contains a comparison between these results for  $F_4$  and the results obtained previously for  $F_1$  and  $F_3$ . This comparison may be slightly erroneous due to the 6-month lapse between measurements. All of the  $T_{op}$  values presented in Table 7-7 have been normalized to standard DSS-13 atmospheric conditions at 32 GHz.

**Table 7-6. Measured zenith operating-noise temperatures corrected for weather and waveguide-loss changes for X-band and Ka-band.**

Configuration	Observation Period (UT)	Average Measured $T_{op}$ (K)	Average Weather During Observation	Computed $T_{atm}^a$ (K)	Computed $L_{atm}^b$	Physical Waveguide Temperature (°C)	$T_{wg}^c$ (K)	Normalized $T_{op}$ (K)
X-band on the ground	03/12/91 1600	22.29	893.6 mbar	2.25	1.0085	13.34	4.58	22.32
	03/13/91 1730		8.9 °C 37.3% RH <sup>d</sup>		(0.037 dB)			
X-band at F <sub>4</sub>	04/27/91 0500	28.84	891.3 mbar	2.27	1.0086	13.96	4.59	28.84
			17.6 °C 26.4% RH		(0.037 dB)			
Ka-band on the ground	04/23/91 1200	83.09	890.8 mbar	10.94	1.0418	5.05	16.77	80.33
	04/24/91 2330		9.96 °C 69.9% RH		(0.178 dB)			
Ka-band at F <sub>4</sub>	05/11/91 0030	93.51	894.1 mbar	8.22	1.0312	7.65	16.77	80.33
	05/12/91 2230		12.6 °C 34.4% RH		(0.133 dB)			

<sup>a</sup> $T_{atm}$  = atmospheric-noise temperature.

<sup>b</sup> $L_{atm}$  = atmospheric loss.

<sup>c</sup> $T_{wg}$  = waveguide-noise temperature.

<sup>d</sup>RH = relative humidity.

Table 7-7. Differential zenith operating-noise temperatures at X-band.

Configurations Differenced	X-Band Delta $T_{op}$ (K)	Ka-Band Delta $T_{op}$ (K)
F <sub>1</sub> – ground	3.2 <sup>a</sup>	7.1 <sup>b</sup>
F <sub>2</sub> – F <sub>1</sub>	Not measured	5.2 <sup>b</sup>
F <sub>3</sub> – F <sub>1</sub>	8.9 <sup>a</sup>	6.8 <sup>b</sup>
F <sub>4</sub> – F <sub>1</sub>	3.3	5.7
F <sub>2</sub> – ground	Not measured	12.3
F <sub>3</sub> – ground	12.1	13.9
F <sub>4</sub> – ground	6.5	12.8

<sup>a</sup> These values obtained from [15].<sup>b</sup> These values obtained from [16].

During Ka-band testing, 8 full days of antenna efficiency measurements were conducted using four radio sources. Figure 7-30 shows the combined antenna efficiency measurements versus elevation angle for Ka-band at the F<sub>4</sub> focal point, with the effects of atmospheric attenuation removed. An average antenna efficiency having a peak of 45.0 percent at an elevation angle of 41.4 deg is also shown. The standard deviation of these data points is 5.0 percent.

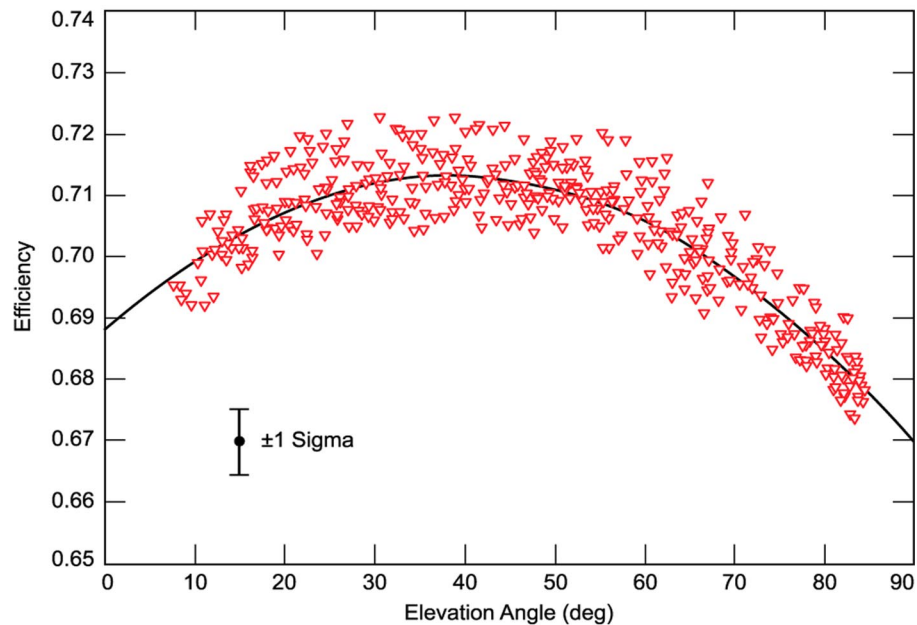
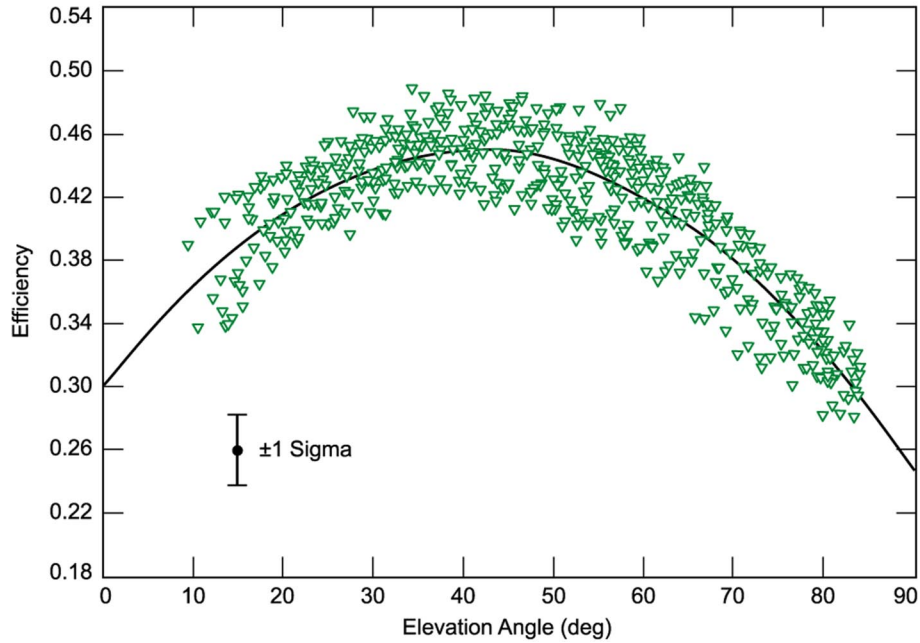


Fig. 7-29. X-band efficiency plot for bypass mode.



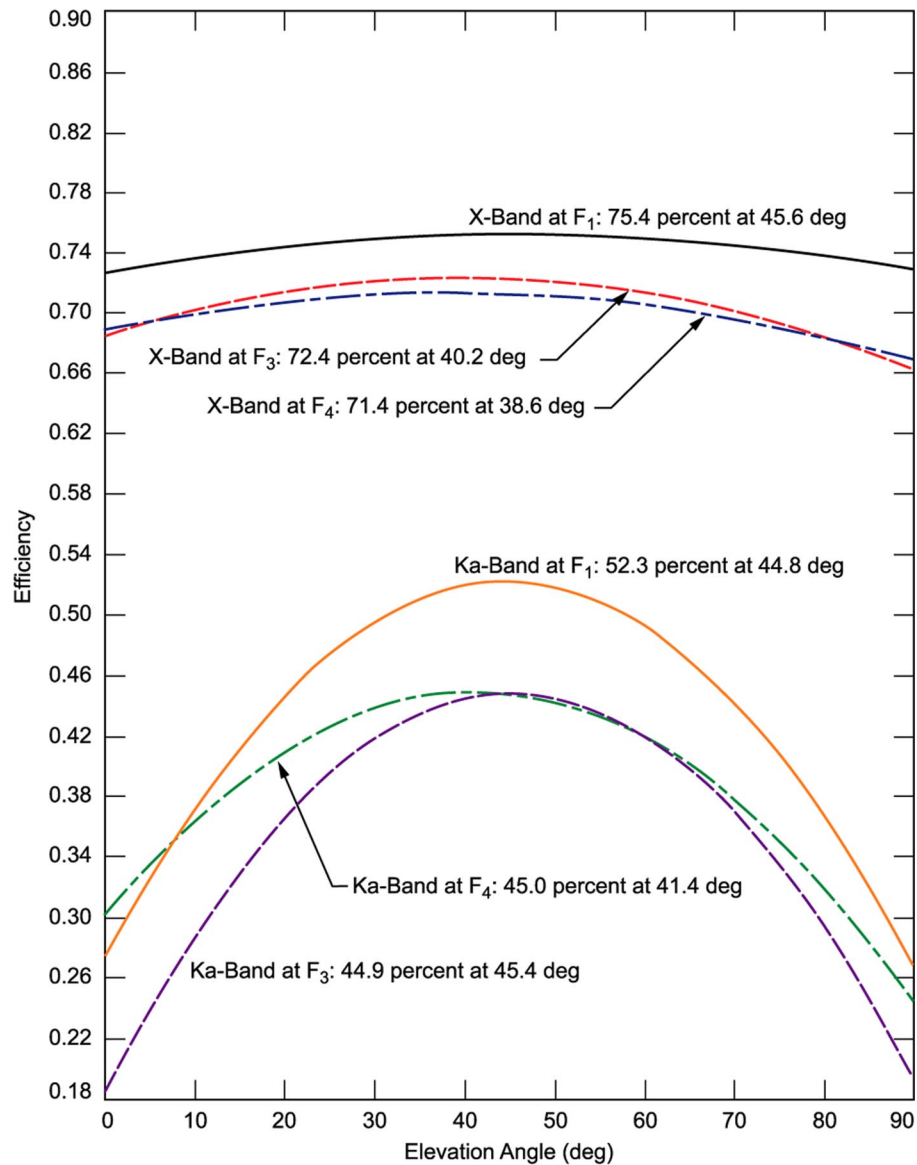
**Fig. 7-30. Ka-band efficiency for bypass mode.**

Figure 7-31 contains the combined results of antenna-efficiency measurements at both X-band and Ka-band for the three focal points,  $F_1$ ,  $F_3$ , and  $F_4$ . The results shown in this figure, like those in Figs. 7-29 and 7-30, have had the effects of atmospheric attenuation removed.

## 7.5 Removal of the Bypass Beam Waveguide

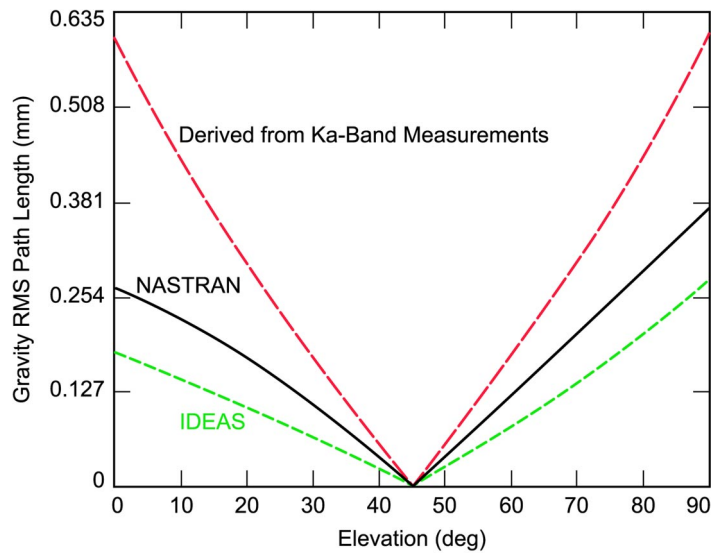
Efficiency measurements showed reasonable X-band performance approximately equivalent to that of the DSN predecessor 34-m HEF antennas. However, Ka-band performance (Figs. 7-27, 7-30, and 7-31) at elevations away from the 45-deg rigging angle was worse than that anticipated from the finite-element method (FEM) model predictions for the effects of gravity loading at these elevations.

Figure 7-32 shows curves for the root-mean-square (rms) surface-path-length-error variation with the antenna elevation angle [24]. The highest valued curve is derived from the Ka-band measurements by converting gain loss to rms, using the Ruze equation [25]. One of the other two curves is derived from the JPL iterative design and antenna structures (IDEAS) [26] FEM software program that was used in the original design. The remaining curve comes from a later NASTRAN [27] FEM program analysis model that incorporated model-



**Fig. 7-31. Comparative results for all the efficiency measurements on the DSS-13 antenna.**

ing refinements and as-built modifications. The errors found from measurements significantly exceed those predicted by the models. The measurement-derived curve amounts to a gain degradation of about 2.6 dB at the extreme elevations, while the NASTRAN model produces only from about 0.6- to 1.1-dB losses. The IDEAS model produces even smaller losses.



**Fig. 7-32. DSS-13 path-length errors from measurements and models.**

Neither of the analytical models accounted for forces from two BWG shroud structures interacting with the backup structure. As shown in Fig. 7-6, one shroud is at the center of the antenna, and the other is a bypass shroud offset from the center. These shrouds are steel shells approximately 8 ft (2.43 m) in diameter with 0.19-in. (4.8-mm)-thick walls that are connected to both the backup structure through bolts and clip angle plate brackets and to the alidade through large-diameter bearings. The models, which were constructed in advance of the eventual detailed design drawings, did not anticipate that shroud loads would interact with the structure. Nevertheless, depending upon how they are connected, loads transmitted by the shroud shells from the alidade into the backup structure can be significant.

A further analytical study examined the potential influence of the shroud-backup interaction forces, and the model with simulated shrouds was capable of approaching the measurements. A major field-measurement strain gauge program was therefore undertaken to measure the actual shroud-backup structure interaction forces.

The primary measurement program consisted of strain gauge measurements and theodolite surface measurements. Supplementary measurements included laboratory load testing of shroud brackets and dial-indicator measurements of relative shroud-antenna motion.

The strain gauge instrumentation and numerical integration provided the magnitudes of the shroud forces. The bypass-shroud forces caused a major disturbance to the surface shape. Analytical FEM models confirmed the sensitivity



of the surface to shroud forces of these magnitudes. Figure 7-33 shows the theodolite measurement points and Fig. 7-34 the best-fit surface errors derived from the theodolite measurements for the difference between the 45-deg rigging angle and the 6-deg elevation angle. The corresponding plot from the FEM model is shown in Fig. 7-35. The effect of the shroud can be clearly seen in the measured data.

The recommendations of the study were either to reduce the interaction of the bypass shroud with the backup structure or else remove the shroud completely. In October 1991, it was proposed to remove the bypass shroud, which no longer was considered to be a microwave requirement, and to free the structure from the associated interaction forces. There appeared to be general agreement that the structure performance would improve through the elimination of the bypass-shroud forces, which acted unsymmetrically on the structure and, therefore, were inconsistent with the desirable objective of homologous struc-

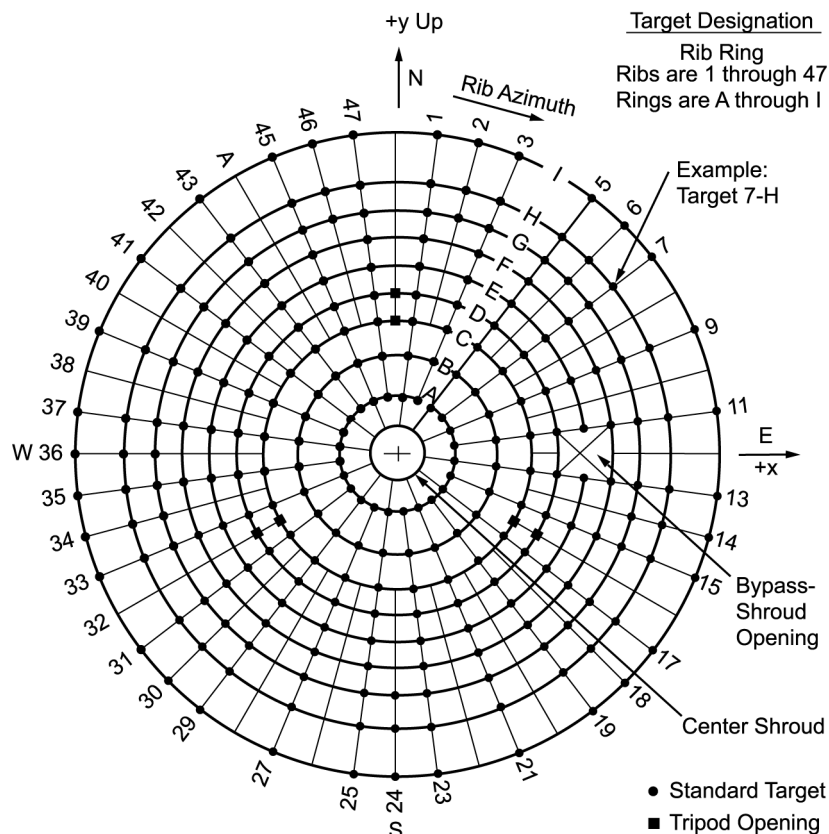
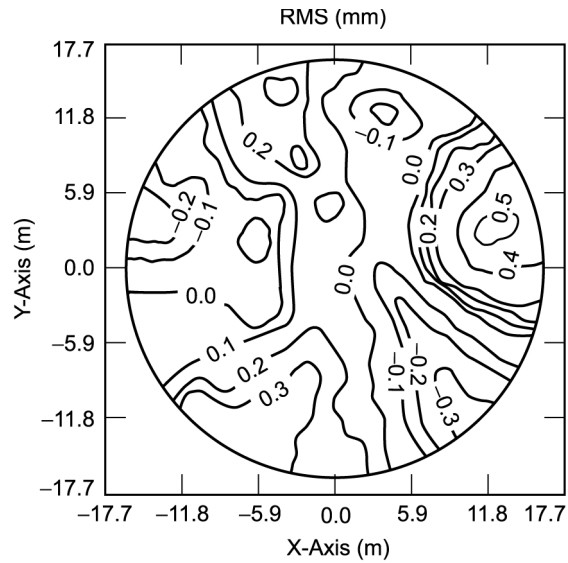
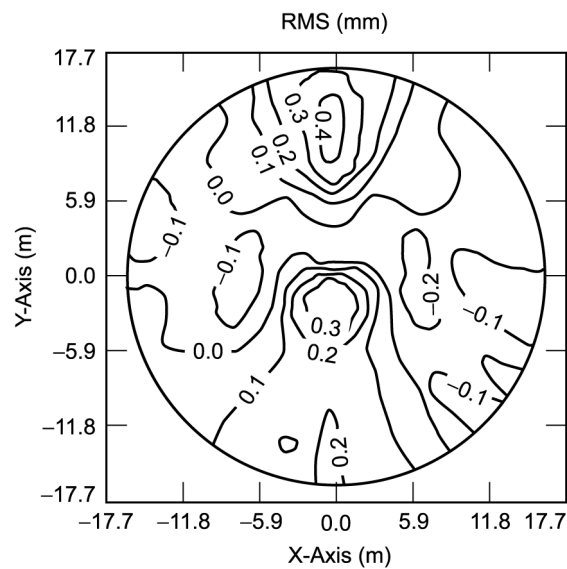


Fig. 7-33. Theodolite measurement points.

ture response. Theodolite and holography measurements clearly established unsymmetrical and nonhomologous surface-distortion patterns.



**Fig. 7-34. Best-fit surface errors, elevation 6–45 deg, from theodolite measurements.**



**Fig. 7-35. Best-fit surface errors, elevation 6–45 deg, from FEM model.**

Ka-band efficiency as a function of elevation angle at  $F_1$  before and after removal of the bypass shroud is shown in Fig. 7-36. Table 7-8 shows the theodolite and holography measurements (rms values) and FEM model predictions. Unfortunately, efficiency roll-off as a function of elevation angle is not substantially different from before removal of the bypass. Thus, even though FEM models the structure with the bypass removed, it still lacks the fidelity to accu-

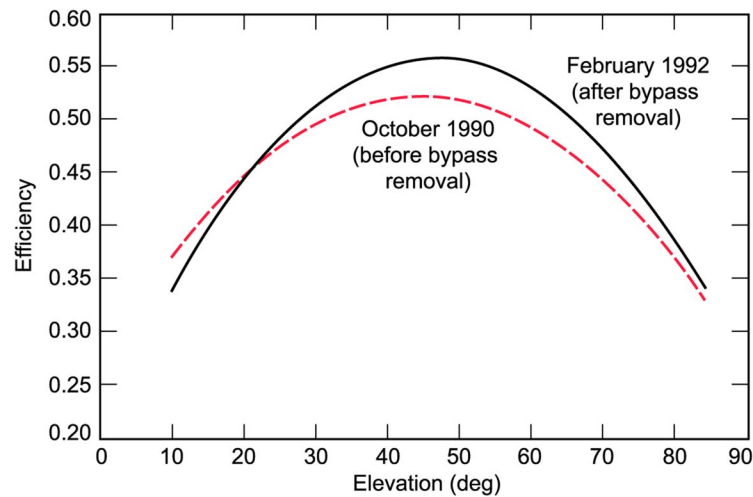


Fig. 7-36. DSS-13 Ka-band efficiency at  $F_1$  before and after bypass removal.

Table 7-8. DSS-13 theodolite measurements and model predictions for gravity loading (best-fit rms half-path-length errors, in mm). Approximate 1-sigma theodolite measurement noise at elevation = 6 deg, noise = 0.41; elevation = 45 deg, noise = 0.23; elevation = 90 deg, noise = 0.18.

Case	Theodolite Measurement	Model Prediction	Holography	Derived from Gain
Elevations 6 deg from 45 deg				
With bypass	0.36	0.18	0.38	0.46
Without bypass	0.46	0.23	0.53	0.48
Elevations 90 deg from 45 deg				
With bypass	0.61	0.38	Not measured	Not measured
Without bypass	0.51	0.36		

rately predict Ka-band performance. Much of the difficulty is traced to the structure joints in that the model does not accurately reflect the actual joint design implemented. A significant effort was made to bring the actual joint design and FEM modeling more in line, and the antenna drawings were updated with the new design. The operational antenna (see Chapter 8 of this monograph) was built with the updated joint design, and performs substantially better than DSS-13. A photograph of the antenna after the bypass removal is shown in Fig. 7-37.

## 7.6 Multifrequency Operation

Most planetary spacecraft use multiple frequencies for both radio science and reliability reasons. Simultaneous dual frequency is provided in the ground system either through the use of a dichroic plate or a multifrequency feed. The initial dual-frequency implementation at DSS-13 utilized dichroic plates. Later implementations of multiple frequencies in BWG systems utilized multiple-frequency feeds.

### 7.6.1 X-/Ka-Band System

The design of the X-/Ka-band system is shown in Figs. 7-38 and 7-39. The optics design uses an additional refocusing elliptical mirror at Ka-band to pro-



Fig. 7-37. DSS-13 after bypass beam-waveguide removal.

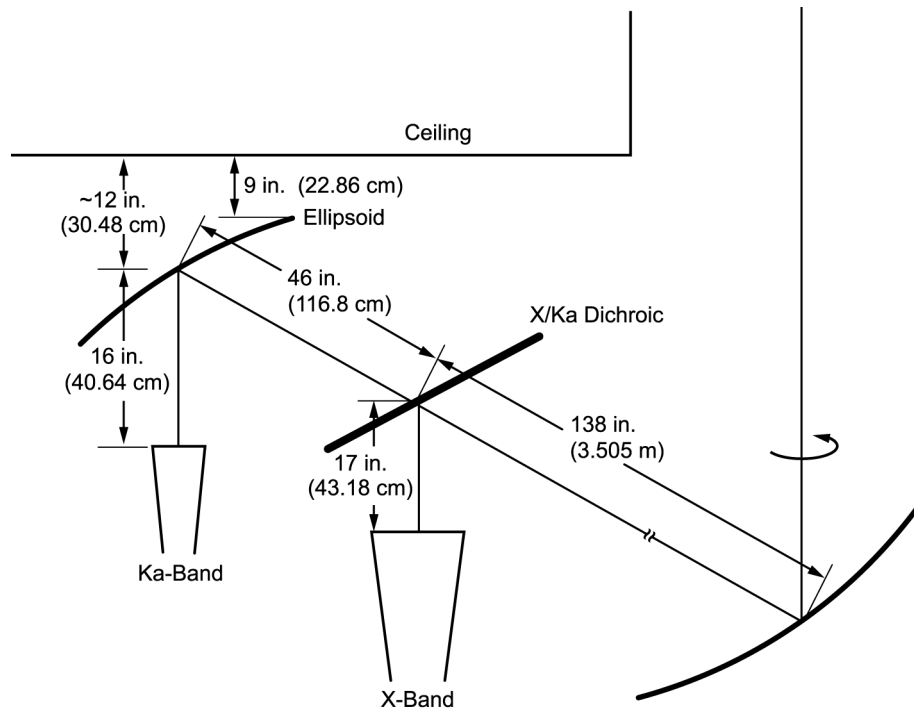


**Fig. 7-38. Optics design configuration of the X- and Ka-band feed system for the DSS-13 Phase II.**

vide sufficient room to fit both receive systems by placing the Ka-band focal point further from the M5 elliptical mirror than the X-band focal point. This is accomplished by putting the Ka-band feed horn at one focus of the ellipse and the other focal point at the input to the M5 magnifying ellipse. In addition, to reduce the spillover loss, the gain of the X- and Ka-band feed horns is increased from the Phase I values of about 22.5 dB, to 25.0 dB and 26.1 dB, respectively. The horn section required to be added on to the X- (as well as Ka-) band (Phase I) horn is identical to the first extended horn section from the JPL standard 22-dB to 29-dB horn (see Fig. 7-40). The ellipse geometry is shown in Fig. 7-41 and the geometry of the dichroic plate in Fig. 7-42. A 20-kW X-band transmitter at 7.7 GHz was also included in the X-band as part of the X-/Ka-band system using a waveguide diplexer. Tests were successfully conducted in the early 1990s with X-band transmitting while simultaneously receiving X- and Ka-bands. There were no noise bursts or intermodulation product signals detected. About the same time, tests were also conducted with the Mars Observer spacecraft to demonstrate the first-ever Ka-band

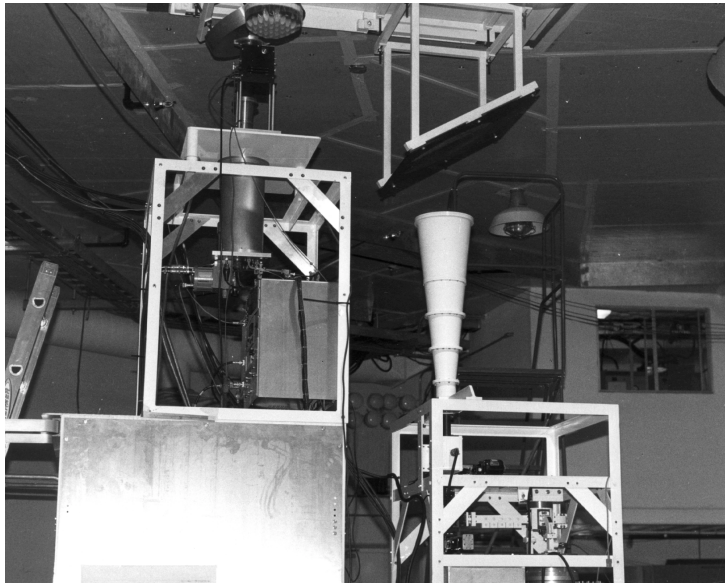


Fig. 7-39. DSS-13 X- and Ka-band feed system.

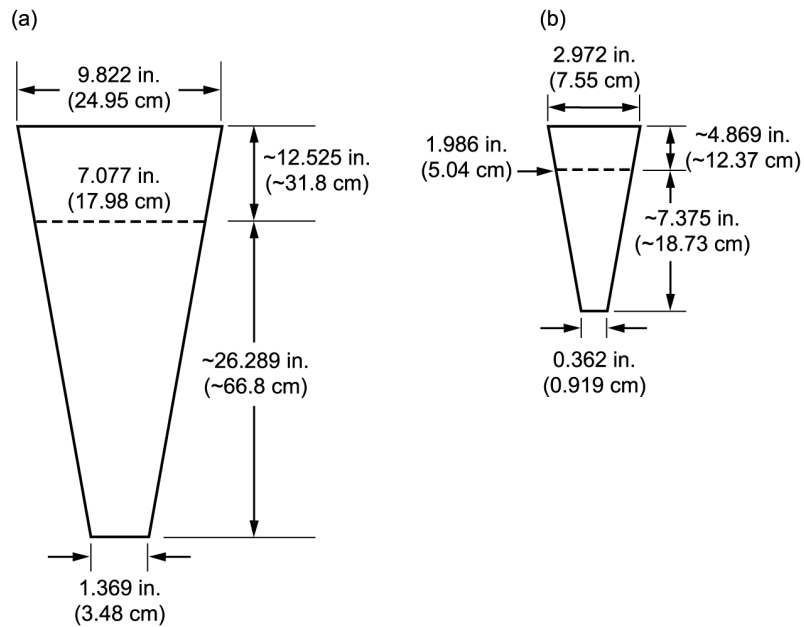
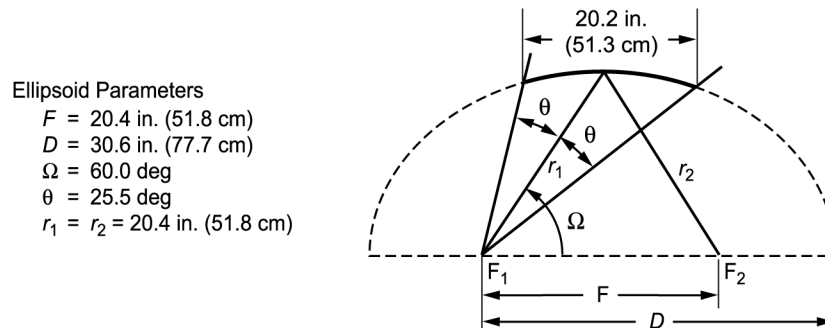


Fig. 7-40. Geometry of the X- and Ka-band feed horns for DSS-13 Phase II.  
All diameters are inside diameters.



**Fig. 7-41. Detail geometry of the ellipsoid above the Ka-band feed horn as shown in Fig. 7-1.**

(33.67-GHz) telemetry reception with a deep-space planetary spacecraft [28,29]. The measured X- and Ka-band efficiencies are shown in Fig. 7-43.

Since the loss of Mars Observer (1993) and the launch of Mars Global Surveyor (1996) spacecraft, tests at Ka-band have continued to assess the quality of the Ka-band link [30,31].

The X-/Ka-band system was subsequently modified to include Ka-band transmit. This was accomplished by adding a Ka-band transmit feed and using a five-layer dichroic plate [32] to separate the transmit and receive Ka-band frequencies. A sketch of the design is shown in Fig. 7-44. Simultaneous Ka-band transmit with Ka- and X-band reception was successfully demonstrated.

### 7.6.2 S-Band Design

As stated earlier, the DSS-13 BWG system was initially designed (Phase I) for operation at 8.45 GHz (X-band) and 32 GHz (Ka-band) and utilized a GO design technique. In Phase II, 2.3 GHz (S-band) was to be added. At S-band, the mirror diameter is less than 20 wavelengths, and it is clearly outside the original GO design criteria.

If a standard 22-dB S-band feed horn were to be placed at the input focus of the ellipse, the BWG loss would be greater than 1.5 dB, due primarily to the fact that, for low frequencies, the diffraction phase centers are far from the GO mirror focus, resulting in a substantial spillover and defocusing loss. This defocusing is especially a problem for the magnifier ellipse, where the S-band phase center at the output of the ellipse is 3 m away from the GO focus.

A potential solution was to redesign the feed horn to provide an optimum solution for S-band. The question was how to determine the appropriate gain and location for this feed.

A straightforward design by analysis would have proved cumbersome because of the large number of scattering surfaces required for the computa-





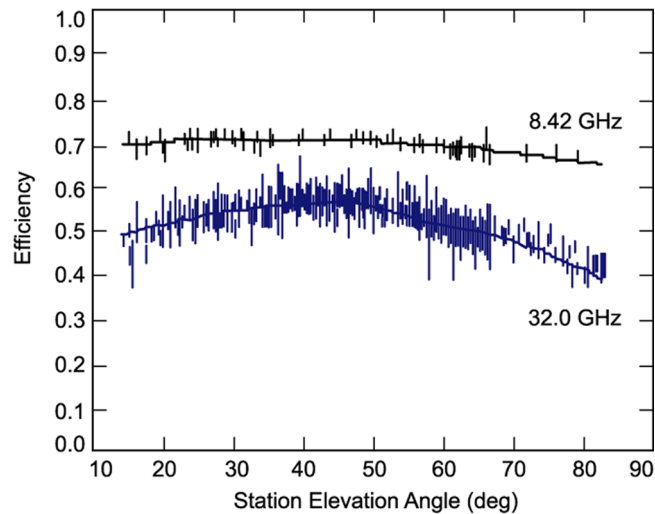


**Fig. 7-43. Antenna efficiency versus elevation angle of the DSS-13 beam-waveguide antenna at X-band (8.4 GHz) and Ka-band (32.0 GHz) along with best-fit curves. Redrawn from [31].**

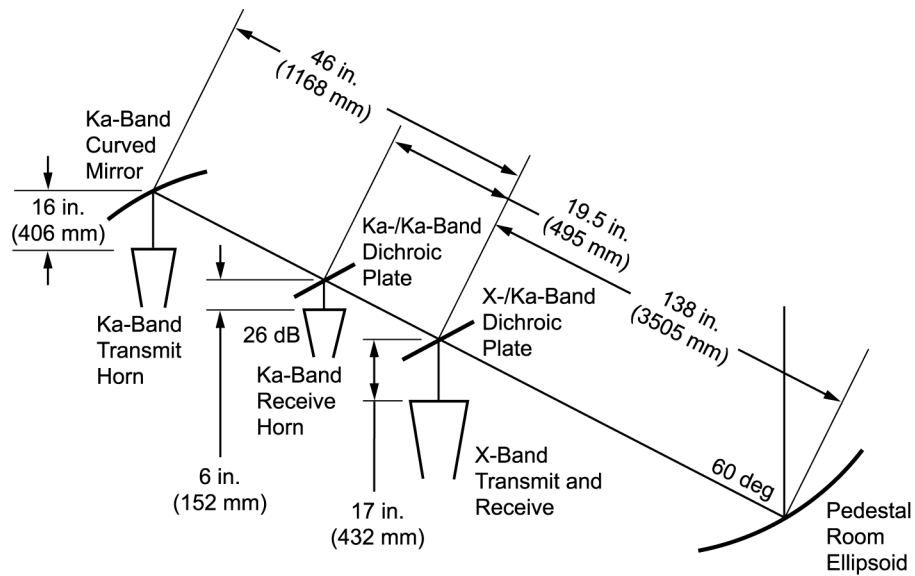


**Fig. 7-44. Ka-band transmit mode optical layout at DSS-13.**

tion. Rather, a unique application was made of the conjugate phase-matching technique to obtain the desired solution [33–35].

A plane wave was used to illuminate the main reflector, and the fields from the currents induced on the subreflector were propagated through the BWG to a plane centered on the input focal point of the M5 ellipse. By taking the complex-conjugate of the currents induced on the focal plane and applying the radiation integral, the far-field pattern of a feed horn that would theoretically maximize antenna gain was obtained.

There was no a priori guarantee that the pattern produced by this method could be produced by a single corrugated feed horn. However, the pattern was nearly circularly symmetric, and the theoretical horn pattern was able to be matched fairly well by an appropriately sized circular corrugated horn.

Figure 7-45 shows the near-field E-plane patterns of the theoretical horn pattern and a 19-dBi circular corrugated horn. The agreement in amplitude and phase is quite good out to  $\theta = 21$  deg, the angle subtended by the beam-magnifier ellipse.

The corrugated horn performance was only 0.2 dB lower than that of the optimum theoretical horn, but about 1.4 dB above that which would be obtained using a standard 22-dBi horn. A system employing the corrugated horn was built and tested and installed in the 34-m BWG antenna as part of a simultaneous S-/X-band receiving system. Figure 7-46 shows the geometry, and Fig. 7-47 a photograph of the actual S-/X-band system.

Table 7-9 lists the PO analysis results of the antenna at S-band. In this table, the spillover of the antenna mirrors, the antenna efficiency, and system-noise temperature are listed for the 19-dBi corrugated feed horn and the theoretical horn pattern predicted by the focal-plane method.

Also, for comparison purposes, the calculated performance of a 22-dBi corrugated horn is presented from [36]. The S-band feed is part of a simultaneous

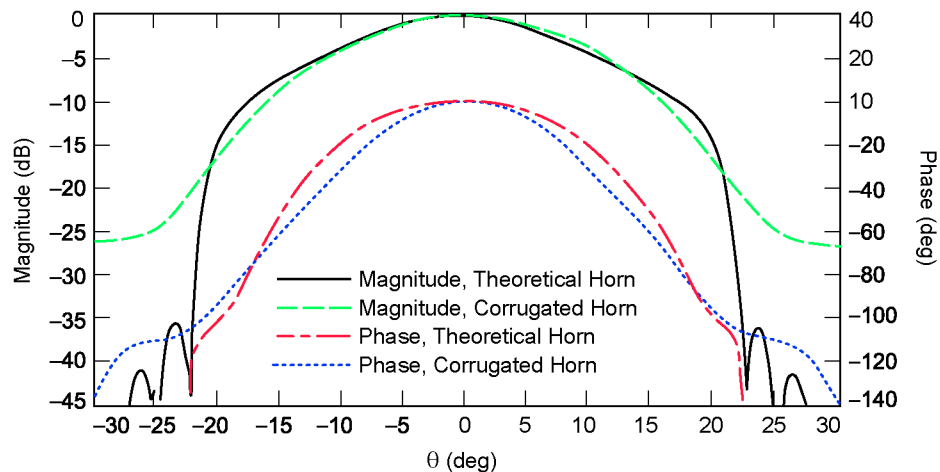


Fig. 7-45. E-plane near-field patterns (input to the ellipse).

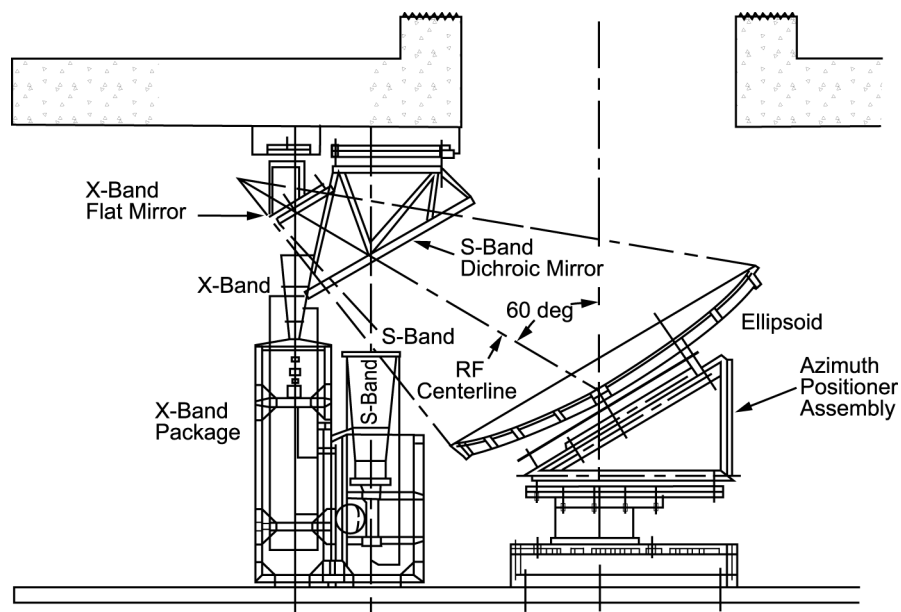


Fig. 7-46. Feed system installed in the beam-waveguide antenna.



Fig. 7-47. DSS-13 S/X-band feed-system geometry.

S-/X-band receive system implemented on the new BWG antenna. The general configuration of the feed system, the detail design, and measured feed system performance are described in [37].

Table 7-9 shows the 34-m BWG antenna predicted S-band efficiency was 68 percent and the measured efficiency was 67.5 percent, demonstrating the successful design and implementation. For comparison, the predicted X-band efficiency (at the rigging angle of 45 deg) was 72.7 percent, and the measured efficiency, including the dichroic plate, was 70.1 percent.

## 7.7 Beam-Waveguide Versatility

After Phase I and at the beginning of Phase II, the basement ellipsoid was placed on a rotating platform to allow easy switching between a number of feed stations assembled in the pedestal room. This versatility of the BWG antenna can be seen in Fig. 7-48. At the time of the photograph, there were five feed stations in the R&D BWG antenna. One was utilized for S-/X-band simultaneous receive operation and one for X-/Ka-band receive and X-band transmit. There was a vernier beam-steering mirror position, which enables conscan operation at Ka-band without scanning the main reflector. There was a seven-element array feed system at this position. The other two positions are for general R&D use and have housed at various times a Ku-band (11.7–12.2-GHz) holography system, the X-band ULNA, and a 49-GHz radio science receiver



Fig. 7-48. Pedestal room at DSS-13.

Table 7-9. S-band physical optics calculations.

Optical Element	Spillover (percent)		
	22-dBi Corrugated Horn	19-dBi Corrugated Horn	Theoretical Horn
M6	0.00	0.41	0.00
M5	2.05	2.46	0.24
M4	1.57	0.70	1.19
M3	5.91	0.73	0.86
M2	5.55	0.96	1.29
M1	1.26	0.26	0.46
Main reflector	0.00	0.94	3.61
Subreflector	0.00	1.14	1.94
Total efficiency (percent)	48.415	68.27	69.502
Total efficiency (dB)	55.102	56.594	56.672

system. Since this photograph was taken, two more positions for R&D use have been added.

## References

- [1] J. W. Layland, R. L. Horttor, R. C., Clauss, J. H. Wilcher, R. J. Wallace, and D. J. Mudgway, "Ka-band Study-1988," *Telecommunications and Data Acquisition Progress Report 42-96*, vol. October–December 1988, [http://tmo.jpl.nasa.gov/progress\\_report/issues.html](http://tmo.jpl.nasa.gov/progress_report/issues.html) Accessed August 2001.
- [2] A. G. Cha, W. A. Imbriale, and J. Withington, "New Analysis of Beam-waveguide Antennas Considering the Presence of the Metallic Tube and its Experimental Verification," *1990 Antennas and Propagation Symposium Digest*, Dallas, Texas, pp. 1506–1509, May 1990.
- [3] A. G. Cha and W. A. Imbriale, "A New Analysis of Beam Waveguide Antennas Considering the Presence of the Metal Enclosure," *IEEE Transactions on Antennas and Propagation*, vol. 40, no. 9, pp. 1041–1046, September 1992.
- [4] J. R. Withington, W. A. Imbriale, and P. Withington, "The JPL Beam-waveguide Test Facility," *1991 Antennas and Propagation Symposium*, Ontario, Canada, pp. 1194–1197, June 1991.

- [5] T. Veruttipong, J. R. Withington, V. Galindo-Israel, W. A. Imbriale, and D. Bathker, "Design Considerations for Beam Waveguide in the NASA Deep Space Network," *IEEE Transactions on Antennas and Propagation*, vol. AP-36, pp. 1779–1787, December 1988.
- [6] T. Veruttipong, W. Imbriale, and D. Bathker, "Design and Performance Analysis of the New NASA Beam Waveguide Antenna," National Radio Science Meeting, Boulder, Colorado, January 3–5, 1990.
- [7] T. Veruttipong, W. Imbriale, and D. Bathker, "Design and Performance Analysis of the DSS-13 Beam Waveguide Antenna," *Telecommunications and Data Acquisition Progress Report 42-101*, vol. January–March 1990, [http://tmo.jpl.nasa.gov/progress\\_report/issues.html](http://tmo.jpl.nasa.gov/progress_report/issues.html) Accessed August 2001.
- [8] M. Mizusawa and T. Kitsuregawa, "A Beamwaveguide Feed Having a Symmetric Beam for Cassegrain Antennas," *IEEE Transactions on Antennas and Propagation*, vol. AP-21, pp. 844–846, November 1973.
- [9] M. Mizusawa, "Effect of Scattering Pattern of Subreflector on Radiation Characteristics of Shaped-Reflector Cassegrain Antenna," *Transactions of the International Electronics and Communications Exhibition*, 52-B, Japan, pp. 78–85, February 1969.
- [10] V. Galindo-Israel, T. Veruttipong, and W. Imbriale, "GTD, Physical Optics, and Jacobi-Bessel Diffraction Analysis of Beam Waveguide Ellipsoids," *IEEE AP-S International Symposium Digest*, vol. 2, Philadelphia, Pennsylvania, pp. 643–646, June 1986.
- [11] V. Galindo-Israel, "Circularly Symmetric Dual-Shaped Reflector Antenna Synthesis with Interpolation Software-User Manual," (internal document) Jet Propulsion Laboratory, Pasadena, California, January 1988.
- [12] T. Y. Otoshi, S. R. Stewart, and M. M. Franco, "A Portable X-Band Front-End Test Package for Beam-Waveguide Antenna Performance Evaluation—Part I: Design and Ground Tests," *Telecommunications and Data Acquisition Progress Report 42-103*, vol. July–September 1990, [http://tmo.jpl.nasa.gov/progress\\_report/issues.html](http://tmo.jpl.nasa.gov/progress_report/issues.html) Accessed August 2001.
- [13] L. Tanida, "An 8.4-GHz Cryogenically Cooled HEMT Amplifier for DSS 13," *Telecommunications and Data Acquisition Progress Report 42-94*, vol. April–June 1988, [http://tmo.jpl.nasa.gov/progress\\_report/issues.html](http://tmo.jpl.nasa.gov/progress_report/issues.html) Accessed August 2001.
- [14] T. Y. Otoshi, S. R. Stewart, and M. M. Franco, "A Portable Ka-Band Front-End Test Package for Beam Waveguide Antenna Performance Evaluation—Part I: Design and Ground Tests," *Telecommunications and Data Acquisition Progress Report 42-106*, vol. April–June 1991, [http://tmo.jpl.nasa.gov/progress\\_report/issues.html](http://tmo.jpl.nasa.gov/progress_report/issues.html) Accessed August 2001.

- [15] T. Y. Otoshi, S. R. Stewart, and M. M. Franco, "A Portable X-Band Front-End Test Package for Beam Waveguide Antenna Performance Evaluation—Part II: Tests on the Antenna," *Telecommunications and Data Acquisition Progress Report 42-105*, vol. January–March 1991, [http://tmo.jpl.nasa.gov/progress\\_report/issues.html](http://tmo.jpl.nasa.gov/progress_report/issues.html) Accessed August 2001.
- [16] T. Y. Otoshi, S. R. Stewart, and M. M. Franco, "A Portable Ka-Band Front-End Test Package for Beam Waveguide Antenna Performance Evaluation – Part II: Tests on the Antenna," *Telecommunications and Data Acquisition Progress Report 42-106*, vol. April–June 1991, [http://tmo.jpl.nasa.gov/progress\\_report/issues.html](http://tmo.jpl.nasa.gov/progress_report/issues.html) Accessed August 2001.
- [17] S. D. Slobin, T. Y. Otoshi, M. J. Britcliffe, L. S. Alvarez, S. R. Stewart, and M. M. Franco, "Efficiency Calibration of the DSS 13 34-Meter Diameter Beam Waveguide Antenna at 8.45 and 32 GHz," *Telecommunications and Data Acquisition Progress Report 42-106*, vol. April–June 1991, [http://tmo.jpl.nasa.gov/progress\\_report/issues.html](http://tmo.jpl.nasa.gov/progress_report/issues.html) Accessed August 2001.
- [18] S. D. Slobin, T. Y. Otoshi, M. J. Britcliffe, L. S. Alvarez, S. R. Stewart, and M. M. Franco, "Efficiency Measurement Techniques for Calibration of a Prototype 34-m Diameter Beam-waveguide Antenna at 8.45 and 32 GHz," *IEEE Transactions on Microwave Theory and Techniques*, vol. 40, no. 6, June 1992.
- [19] M. J. Britcliffe, editor, "DSS-13 Beam Waveguide Antenna Project: Phase I Final Report," JPL D-8451 (internal document), Jet Propulsion Laboratory, Pasadena, California, pp. 5–12, March 1991.
- [20] M. S. Esquivel, "Optimizing the G/T Ratio of the DSS-13 34-meter Beam Waveguide Antenna," *Telecommunications and Data Acquisition Progress Report 42-109*, vol. January–March 1992, [http://tmo.jpl.nasa.gov/progress\\_report/issues.html](http://tmo.jpl.nasa.gov/progress_report/issues.html) Accessed August 2001.
- [21] W. Imbriale, W. Veruttipong, T. Otoshi, and M. Franco, "Determining Noise Temperatures in Beam Waveguide Systems," *Telecommunications and Data Acquisition Progress Report 42-116*, vol. October–December 1993, [http://tmo.jpl.nasa.gov/progress\\_report/issues.html](http://tmo.jpl.nasa.gov/progress_report/issues.html) Accessed August 2001.
- [22] G. W. Glass, G. G. Ortiz, and D. L. Johnson, "X-band Ultralow-Noise Maser Amplifier Performance," *Telecommunications and Data Acquisition Progress Report 42-116*, vol. October–December 1993, [http://tmo.jpl.nasa.gov/progress\\_report/issues.html](http://tmo.jpl.nasa.gov/progress_report/issues.html) Accessed August 2001.
- [23] S. Stewart, "DSS-13 Beam-Waveguide Antenna Performance in the Bypass Mode," *Telecommunications and Data Acquisition Progress Report 42-108*, vol. October–December 1991, [http://tmo.jpl.nasa.gov/progress\\_report/issues.html](http://tmo.jpl.nasa.gov/progress_report/issues.html) Accessed August 2001.



- [24] R. Levy, "DSS-13 Antenna Structure Measurements and Evaluation," JPL D-8947 (internal document), Jet Propulsion Laboratory, Pasadena, California, October 1, 1991.
- [25] J. Ruze, "Antenna Tolerance Theory-A Review," *Proceedings of the IEEE*, vol. 54, no. 4, pp. 633–640, April 1966.
- [26] R. Levy and D. Strain, "JPL-IDEAS, Iterative Design and Antenna Structures," COSMIC, NPO 17783, University of Georgia, Athens, Georgia, October 1988.
- [27] *The NASTRAN Theoretical Manual*, COSMIC, NASA SP 221(06) University of Georgia, Athens, Georgia, January 1981.
- [28] D. D. Morabito and L. Skjerve, "Analysis of Tipping-Curve-Measurements Performed at the DSS-13 Beam-Waveguide Antenna at 32.0 and 8.45 GHz," *Telecommunications and Data Acquisition Progress Report 42-122*, vol. April–June 1995, [http://tmo.jpl.nasa.gov/progress\\_report/issues.html](http://tmo.jpl.nasa.gov/progress_report/issues.html) Accessed August 2001.
- [29] D. Morabito, "The Efficiency Characterization of the DSS-13 34-Meter Beam-Waveguide Antenna at Ka-Band (32.0 and 33.7 GHz) and X-band (8.4 GHz)," *Telecommunications and Data Acquisition Progress Report 42-125*, vol. January–March 1996, [http://tmo.jpl.nasa.gov/progress\\_report/issues.html](http://tmo.jpl.nasa.gov/progress_report/issues.html) Accessed August 2001.
- [30] D. Morabito, S. Butman, and S. Shambayati, "The Mars Global Surveyor Ka-Band Link Experiment (MGS/KaBLE II)," *Telecommunications and Data Acquisition Progress Report 42-137*, vol. January–March 1999, [http://tmo.jpl.nasa.gov/progress\\_report/issues.html](http://tmo.jpl.nasa.gov/progress_report/issues.html) Accessed August 2001.
- [31] D. Morabito, "Characterization of the 34-Meter Beam-Waveguide Antenna at Ka-band (32.0 GHz) and X-band (8.4 GHz)," *IEEE Antennas and Propagation Magazine*, vol. 41, no. 4, pp. 23–34, August 1999.
- [32] J. C. Chen, P. H. Stanton, and H. F. Reilly, Jr., "A Prototype Ka/Ka-Band Dichroic Plate With Stepped Rectangular Apertures," *Telecommunications and Data Acquisition Progress Report 42-124*, vol. October–December 1995, [http://tmo.jpl.nasa.gov/progress\\_report/issues.html](http://tmo.jpl.nasa.gov/progress_report/issues.html) Accessed August 2001.
- [33] W. A. Imbriale, "Solutions to Low-Frequency Problems with Geometrically Designed BWG Systems," National Radio Science Meeting, Boulder, Colorado, p. 60, January 7–10, 1992.
- [34] W. A. Imbriale and M. S. Esquivel, "A Novel Design Technique for Beam-waveguide Antennas," 1996 *IEEE Aerospace Applications Conference*, Aspen, Colorado, vol. 1, pp. 111–119, February 3–10, 1996.



- [35] W. A. Imbriale, M. S. Esquivel, and F. Manshadi, "Novel Solutions to Low-Frequency Problems with Geometrically Designed Beam-Waveguide Systems," *IEEE Transactions on Antennas and Propagation*, vol. 46, no. 12, pp. 1790–1796, December 1998.
- [36] T. Cwik and J. C. Chen, "DSS-13 Phase II Pedestal Room Microwave Layout," *Telecommunications and Data Acquisition Progress Report 42-106*, vol. April–June 1991, [http://tmo.jpl.nasa.gov/progress\\_report/issues.html](http://tmo.jpl.nasa.gov/progress_report/issues.html) Accessed August 2001.
- [37] F. Manshadi, "The S/X-Band Microwave Feed System for NASA's First Beam-waveguide Antenna," *1996 IEEE Aerospace Applications Conference*, Aspen, Colorado, February 3–10, 1996.